

1 **Influence of salt-related of crustal mechanical layering on the seismic**  
2 **potential of active faults: insights Insights from the southwestern Valencia**  
3 **Trough (W Mediterranean)**

4  
5 Martin-Rojas, Iván<sup>1</sup>

6 Ramos, Adrià<sup>2,1</sup>

7 De Ruig, Menno<sup>2</sup>

8 Medina-Cascales, Iván<sup>1</sup>

9 Santamaría-Pérez, Eva<sup>1</sup>

10 Alfaro, Pedro<sup>1</sup>

11  
12 1 Dpto. de Ciencias de la Tierra y del Medio Ambiente, Universidad de Alicante,  
13 Campus San Vicente s/n, 03690, San Vicente del Raspeig, Alicante.

14 [ivan.martin@ua.es](mailto:ivan.martin@ua.es)

15 2. Departament de Botànica i Geologia, Universitat de València, 46010 Burjassot,  
16 Valencia, Spain

17 32. Lithologic, 2582 LD The Hague, The Netherlands.

18 [lithologic.mail@gmail.com](mailto:lithologic.mail@gmail.com) Oropesa BV, Van Bteiswijkstraat 183, 2582 LD The  
19 Hague, Netherlands. [menno.deruig@gmail.com](mailto:menno.deruig@gmail.com)

20  
21 Corresponding author: Martin-Rojas, Iván

22 Dpto. de Ciencias de la Tierra y del Medio Ambiente, Universidad de Alicante,  
23 Campus San Vicente s/n, 03690, San Vicente del Raspeig, Alicante.

24 [ivan.martin@ua.es](mailto:ivan.martin@ua.es)

Con formato: Español (España)

27 **Short summary**

28 This study investigates the main active faults located within the southwestern  
29 Valencia Trough, an offshore region east of the Spanish coast. Utilizing subsurface  
30 data, we identify and characterize the 3D geometry of several of these faults for the  
31 first time. Given that active faults pose a significant natural hazard ~~due~~owing to their  
32 potential to generate earthquakes, we also assess the seismic potential of the faults  
33 within the southwestern Valencia Trough.

34

35 **ABSTRACT**

36

37 We present a structural and seismotectonic analysis of active faults in the  
38 southwestern Valencia Trough (western Mediterranean) on the basis of subsurface  
39 datasets. In our study, we identify and characterise three major active faults: the  
40 Cullera Fault, with a long-term slip rates that vary over time between  $0.15 \pm 0.1$   
41 mm/yr and  $0.4 \pm 0.1$  mm/yr; the oblique Albufera Fault, with a long-term slip rate of  
42  $0.2 \pm 0.1$  mm/yr; and the normal Valencia Fault.

43 The seismogenic character of the southwestern Valencia Trough is controlled by a  
44 mechanically weak layer consisting of Triassic evaporites. This weak layer induces  
45 partial ~~to~~ complete decoupling between the suprasalt and subsalt successions,  
46 leading to two distinct mechanisms driving fault displacement: tectonic activity and  
47 salt withdrawal. A quantitative evolutionary analysis of the Cullera Fault reveals that  
48 these two mechanisms occur alternately over time.

49 The presence of a mechanically weak layer has implications for seismicity.  
50 Earthquakes can nucleate within both sub- and suprasalt successions, with total or  
51 partial decoupling influencing rupture propagation. We discuss how these two  
52 scenarios lead to different earthquakes and thus impact the seismic hazard of a  
53 region. Empirical source-scaling relationships, which are commonly used to  
54 estimate the seismogenic potential of active faults, generally assume a  
55 homogeneous seismogenic crust. To address this limitation, we propose a  
56 methodological approach based on the use of the aspect ratio. Using this method,  
57 the maximum magnitudes for suprasalt ruptures are 5.8-6.4, 5.4-6.2, and 5.1-5.9 for  
58 the Cullera, Valencia, and Albufera faults, respectively. These values are 11-25%  
59 lower than those obtained by considering the rupture of the entire seismogenic  
60 crust. Our findings highlight the need to incorporate stratigraphic mechanical  
61 layering into seismic hazard assessments, particularly in salt-influenced tectonic  
62 settings.

63

64

Con formato: Interlineado: 1.5 líneas

65 **1. Introduction**

66 Seismic hazard analyses are often performed by scaling relationships. These  
67 relationships are regressions in which the seismogenic potential of active faults is  
68 derived from geometric parameters of the fault, such as the potential fault rupture  
69 length or area (Stirling et al., 2013). Pioneering works on scaling relationships began  
70 in the 1970s (Kanamori & Anderson, 1975; Geller, 1976). The regressions of Wells &  
71 Coppersmith (1994) represent a milestone in the application of scaling  
72 relationships, as they included a very large dataset of historical earthquakes. The  
73 equations proposed by Wells & Coppersmith became a standard for determining  
74 the seismogenic potential of active faults. Subsequently, other scaling relationships  
75 have been proposed, accounting for factors such as the tectonic environment, fault  
76 dip, or seismogenic thickness (Stirling et al., 2002 and 2013; Leonard 2010 and  
77 2014; Huang et al., 2024, among many others).

78 Most scaling relationships employed to evaluate crustal earthquakes correlate the  
79 moment magnitude ( $M_w$ ) with the fault dimensions (length, width, and/or area).  
80 Some of these scaling relationships consider the fault width vs. fault dip growth of  
81 ruptures for large earthquakes, as rupture width is limited by the maximum depth of  
82 the seismogenic crust (Leonard, 2010; Yen and Ma, 2011; Leonard, 2014; Cheng et  
83 al., 2019). ~~However, Standard relationships include data from hundreds or even~~  
84 ~~thousands of events. Therefore, the influence in these relationships of potential~~  
85 ~~mechanical heterogeneities within the seismogenic crust should be implicit.~~  
86 ~~However, because of the large amount of data, the mean regressions average out~~  
87 ~~the less common situations, as the presence of a mechanical weak layer. Therefore,~~  
88 ~~as a consequence of this averaging, these empirical relationships do not consider~~  
89 ~~permit to compute~~ the influence of potential heterogeneities within the seismogenic  
90 crust. ~~These heterogeneities, which~~ could control the vertical propagation of  
91 ruptures and, therefore, the magnitude of earthquakes.

92 Here, we present an analysis of several subsurface datasets, including high-  
93 resolution seismic profiles, from the southwestern Valencia Trough. We identify and  
94 characterise the main active faults in this region, and we carry out a detailed  
95 geometric description. The results of this analysis also emphasize that this region is

96 characterised by a mechanically weak layer within the seismogenic crust. After  
97 mapping the main faults, we apply conventional scaling relationships to evaluate  
98 the potential magnitudes of future earthquakes. We propose a methodological  
99 approach for integrating the effects of mechanically weak layers—such as Triassic  
100 evaporites—into routine seismic hazard assessments, highlighting the need to  
101 refine existing scaling relationships in tectonically complex settings.

102 **2. Tectonic setting**

103 The Valencia Trough is an extensional basin located in the western Mediterranean  
104 region (Fig. 1). This basin is the result of polyphase tectonic evolution spanning from  
105 the Triassic to the present day, as it is located between the Betic–Balearic fold-and-  
106 thrust belt to the south, the Iberian Chain to the west, and the Catalan Coastal  
107 Ranges to the north (De Ruig, 1992; Guimerà & Álvaro, 1990; Maillard & Mauffret,  
108 1999; Roca & Desegaulx, 1992; Roca et al., 2004; Vergés & Fernández, 2012). The  
109 tectonic evolution of the Valencia Trough is also partially influenced by extension  
110 related to the retreat of the Maghrebian–Ligurian Tethys subduction slab (Etheve et  
111 al., 2016; Faccenna et al., 2004; Jolivet & Faccenna, 2000; Maillard & Mauffret, 1999;  
112 Rehault et al., 1984; Roca et al., 1999; Séranne, 1999; van Hinsbergen et al., 2014).

Con formato: Inglés (Estados Unidos)

113 The Valencia Trough (Fig. 1) underwent a Mesozoic rifting process related to the  
114 Iberian intraplate rift and the opening of the Western Tethys (Arche and López-  
115 Gómez, 1996; Nebot and Guimerà, 2018; Ramos et al., 2023; Salas et al., 2001). This  
116 process led to the formation of NW–SE and NE–SW high-angle faults offsetting  
117 the pre-Mesozoic basement and to the deposition of a 5–15-km-thick Upper  
118 Jurassic–Lower Cretaceous succession.

Con formato: Inglés (Estados Unidos)

Con formato: Inglés (Estados Unidos)

119 During the Late Cretaceous, the onset of convergence between Nubia and Eurasia  
120 caused the transition from a Mesozoic extensional tectonic regime to successive  
121 compressional and extensional stages (Roca, 2001; Salas et al., 2001; Vergés and  
122 Sàbat, 1999). From the late Eocene to the Oligocene, the Valencia Trough was  
123 dominated by shortening. Onshore, this episode led to the formation of the  
124 intraplate Iberian Chain and Catalan Coastal Ranges (Gaspar-Escribano et al.,  
125 2004; Geel, 1995; Guimerà and Álvaro, 1990).

126 From the late Oligocene to the middle Miocene, the western Mediterranean region  
127 was subsequently affected by an extensional regime, driven by the complex  
128 interplay between the European–Cenozoic rift system (e.g., Séranne, 1999) and the  
129 rollback of the Maghrebian–Ligurian Tethys slab (Faccenna et al., 2004; van  
130 Hinsbergen et al., 2014). This extensional phase led to the formation of the Liguro-  
131 Provençal and Algerian Basins, as well as the Valencia Trough. However, subsidence  
132 in the southwestern Valencia Trough during this period cannot be accounted for by

133 rifting, due to the limited occurrence of Cenozoic basement extensional faults  
134 (Roca and Guimerà, 1992). Therefore, extension has been interpreted as due to the  
135 collapse of a back-arc transient uplift event (Fang et al., 2021).

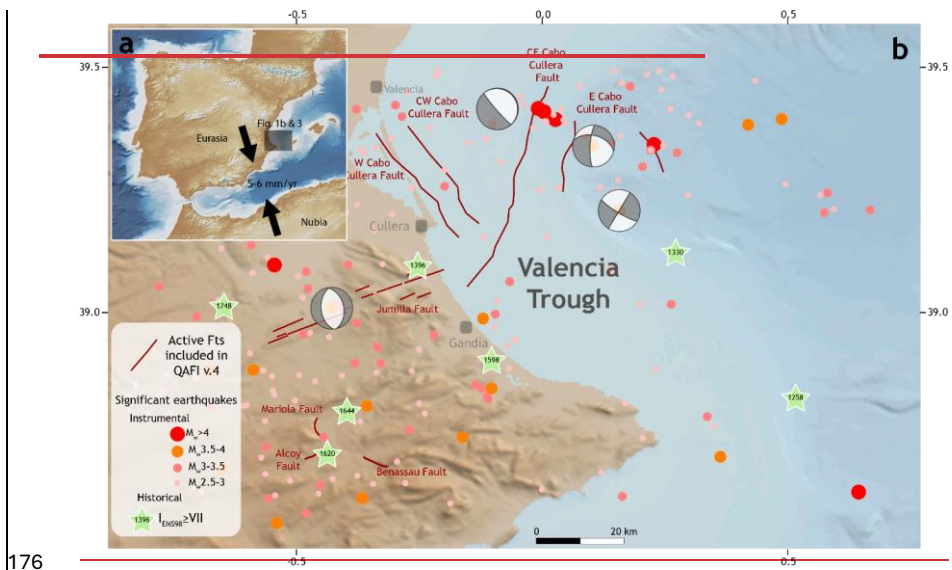
136 The extension in the Valencia Trough occurred immediately before or synchronously  
137 with the formation of the compressional Betic Cordillera. This compressional  
138 deformation is well expressed by a thin-skinned fold-and-thrust system observed in  
139 the Eastern Betic Cordillera (De Ruig, 1995; Sàbat et al., 2011) and in the Balearic  
140 Promontory (Mallorca and Ibiza Islands). At the same time, significant magmatic  
141 activity took place in the area. ~~This magmatism, and~~ was divided into two phases:  
142 (1) late Oligocene to Serravallian calc-alkaline activity and (2) Tortonian to present  
143 alkaline volcanic activity (Martí et al., 1992).

144 From the Pliocene to the present, the tectonic setting in the Valencia Trough has  
145 been dominated by NE–SW extension, as indicated by focal mechanisms (Stich et  
146 al., 2010) and broad regional global navigation satellite system (GNSS) analyses  
147 (Stich et al., 2006). This extension has been related to thermal subsidence (Roca,  
148 1992, 1996, and 2001; Roca and Guimerà, 1992; Roca et al., 1999a; Gaspar-  
149 Escribano et al., 2004) and has been interpreted as the final stage of an aborted rift  
150 event responsible for the ENE motion of the Balearic promontory (Palano et al.,  
151 2015). Several normal active faults have been defined in the southwestern Valencia  
152 Trough thus far (Fig. 1): the Western Cabo Cullera Fault, Central–Western Cabo  
153 Cullera Fault, Central–Eastern Cabo Cullera Fault, Eastern Cabo Cullera Fault and  
154 Southwest Columbretes Fault (Perea, 2006). Some of these faults were previously  
155 recognised from vintage seismic lines (Diaz del Rio et al., 1986; Roca, 1992, 1996;  
156 Perea, 2006; Maillard & Mauffret, 2013), but fault traces and geometry were defined  
157 only very approximately. Similarly, the slip rates derived from the displacement of  
158 Plio-Quaternary seismic reflectors observed in the vintage seismic lines present  
159 high uncertainties ( $0.02 \pm 0.01$  mm/yr; Perea, 2006). In the Valencia Trough,  
160 seismicity is characterised by low- to moderate-magnitude events (Fig. 1). The few  
161 available focal mechanisms (Stich et al., 2010; IGN, 2025) indicate a normal—  
162 oblique or strike slip kinematics, although these focal mechanisms present high  
163 uncertainties, mainly because they occur at long distances from seismic stations

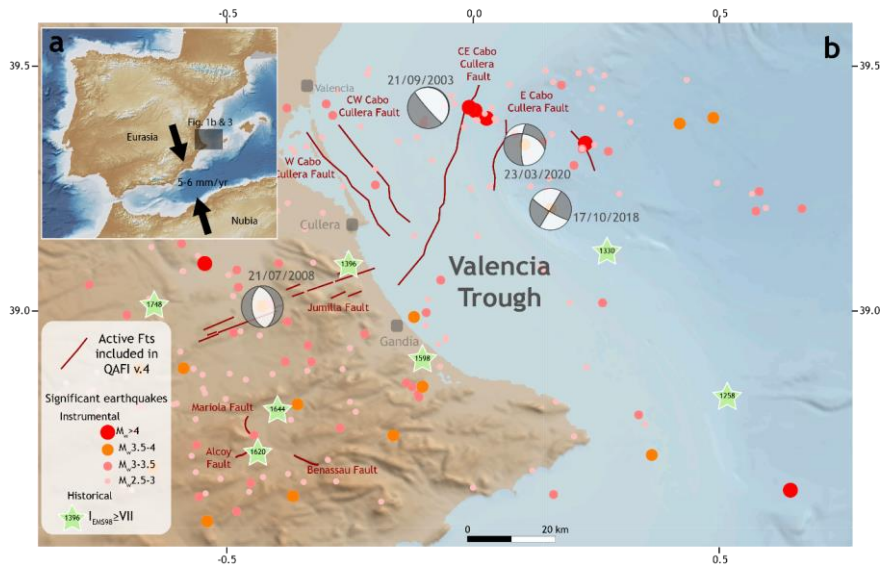
Con formato: Inglés (Estados Unidos)

164 and are registered with significant azimuthal gaps (González, 2017). According to  
165 the data published by the Spanish Earthquake Catalogue (IGN, 2025), this  
166 seismicity is very shallow, as most of the events are assigned depths of less than 10  
167 km (Fig. 2). However, ~~once again~~, these data should be taken with caution, as the  
168 depths assigned to these earthquakes present high uncertainties (González, 2017).

169 In the onshore domain located west of the Valencia Trough, only one major active  
170 structure, namely, the Jumilla Fault, has been postulated (García-Mayordomo et al.,  
171 2012), together with other minor active faults (Alcoy, Mariola, and Benasau Faults).  
172 In this onshore area, several significant historical earthquakes have occurred, such  
173 as the 1396 Tavernes ( $I_{EMS98}$ =VIII-IX), 1620 Alcoy ( $I_{EMS98}$ =VIII-IX), 1644 Muro ( $I_{EMS98}$ =V)  
174 and 1748 Estubeny ( $I_{EMS98}$ =IX) earthquakes (Martínez Solares and Mezcua, 2002;  
175 IGN, 2025; Buforn et al., 2105; Buforn & Udías, 2022).



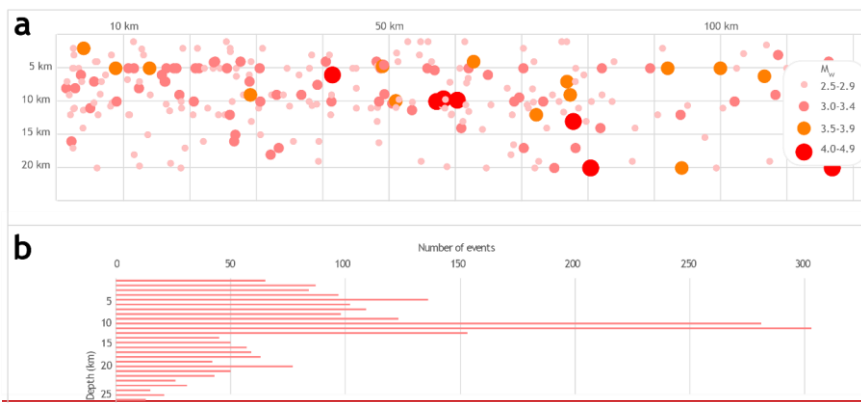
176



177

178 Fig. 1. a. Location of the Valencia Trough. Convergence vectors between Nubia and  
 179 Eurasia are after DeMets et al., 1994; McClusky et al., 2003; Nocquet, 2012;  
 180 Nocquet & Calais, 2003; Pérez-Peña et al., 2010; Serpelloni et al., 2007; Stich et al.,  
 181 2006. b. Seismotectonic map of the southwestern Valencia Trough and surrounding  
 182 areas. Fault traces from Quaternary-Active Faults of Iberia database (García-  
 183 Mayordomo et al., 2012)

184



185



186

187 Fig 2. Seismicity of  $M_w > 2.5$  in the southwestern Valencia Trough shallower than 20  
 188 km since 1950 from the *Instituto Geográfico Nacional* database (IGN, 2025). a.  
 189 Distribution of the depth of seismicity. Horizontal-The horizontal axis represents  
 190 distance along the southwestern Valencia Trough in a SW-NE direction (from  
 191 the SW shoreline to the NE Mediterranean Sea). b. Energy (from magnitude) and  
 192 depth histogram. In both graphics events with 0 km of the assigned depth are not  
 193 represented (fixed depth).

Con formato: Fuente: Cursiva

Con formato: Inglés (Estados Unidos)

Con formato: Inglés (Estados Unidos)

Con formato: Inglés (Estados Unidos)

### 194 3. Methods-Data

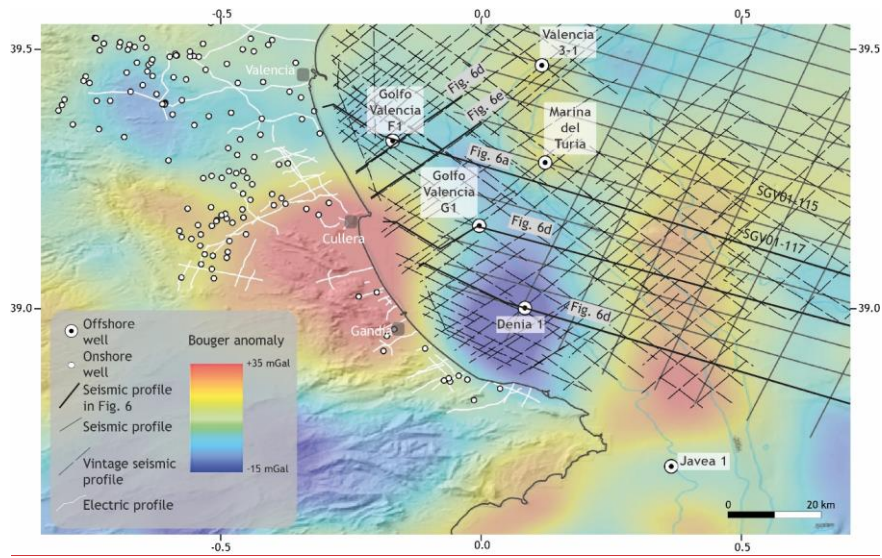
195 The interpretation of the offshore area is based on mainly 2D multichannel seismic  
196 reflection data calibrated with well data (Fig. 3). The central part of the study area is  
197 covered by a high-quality seismic survey acquired by Fugro-Geoteam with the RV  
198 Geo Baltic, processed by Robertson Research International Ltd. in 2002. The survey  
199 consists of 30 seismic sections with an average length of 90 km (totalling  
200 approximately 2,800 km). They are oriented WNW–ESE and NNE–SSW, with  
201 maximum spacings of 13 km and 6 km, respectively. The details regarding the  
202 acquisition and processing parameters can be found in Cameselle & Urgeles (2017).  
203 Most of the area affected by Plio-Quaternary faulting nearer to the coast is covered  
204 only by vintage 2D seismic lines from the late 1970s, acquired by various operators,  
205 which are publicly available upon request in the Instituto Geológico y Minero de  
206 España (IGME-CSIC) (<http://info.igme.es/sigeof/>). More than 100 of these seismic  
207 lines, with a total line length of approximately 2,500 km, were selected for mapping;  
208 although the quality of these lines varies from moderate to poor, the high-density  
209 grid spacing (varying from 1 to 3.5 km) allows fault mapping with reasonable  
210 confidence. The seismic interpretation was performed in two-way travel time (TWT)  
211 by using Move software (by Petex). The seismic dataset was converted to depths  
212 using velocity data derived from the Expanded Spread Profile (ESP) 7 (Pascal et al.,  
213 1992; Torné et al., 1992). A second-order polynomial trend was applied to establish  
214 time–depth relationships, ensuring strong correlation with the well data, similar to  
215 the methodologies of Fang et al. (2021).

216 The interpretation of seismic horizons is calibrated by 9 offshore petroleum  
217 exploration wells, all of which penetrate the entire Neogene section and whose  
218 bottoms are in Mesozoic rocks. Original well reports, log data (lithology, dipmeter,  
219 gamma–ray, sonic and resistivity data) and palaeontological data (from cuttings and  
220 sidewall cores) were retrieved from the IGME-CSIC archive  
221 (<https://info.igme.es/hidrocarburos/>). Well-to-seismic ties were established by  
222 integrating the sonic logs and using synthetic seismograms from end-of-well  
223 reports. Palaeontological analyses and range charts from the original well reports

Código de campo cambiado

Código de campo cambiado





238

239 Fig. 3. Geophysical dataset used in this work. Filtered Bouguer anomaly data after  
 240 Getech (2015). The location is shown in figure 1.

241

#### 242 4. Stratigraphy

243 The general stratigraphic arrangement of the southwestern Valencia Trough (Fig. 4)  
244 consists of a rigid Palaeozoic–Middle Triassic basement overlain by a 1.5–7-km  
245 Upper Triassic–Quaternary stratigraphic cover. Here we present a new detailed  
246 stratigraphic framework for the late Miocene–Quaternary of the southern Valencia  
247 Trough. The definition of the pre-Neogene stratigraphic units presented in this work  
248 is based on mainly previous literature and our analysis of well data, as well as  
249 outcrops in the mainland for the most recent sediments.

250 The Upper Triassic succession (Fig. 4) consists of evaporites, shales and dolomites  
251 (Keuper Facies) (Vargas et al., 2009). The Upper Triassic deposits are overlain by  
252 ~~shallow-water dolomites and anhydrites deposited from the~~ Early to Middle Jurassic  
253 ~~to Late Cretaceous carbonates and marls~~ (Salas et al., 2001). ~~The Upper Jurassic~~  
254 ~~and Lower Cretaceous successions are represented by platform carbonates that~~  
255 ~~grade to marls basinwards and are overlain by middle-late Albian to Late~~  
256 ~~Cretaceous carbonates. The top of the Mesozoic succession corresponds to an~~  
257 erosive, angular unconformity that is directly overlain by Neogene deposits.  
258 ~~Cenozoic infilling has been broadly studied in recent decades (e.g., Arche et al.,~~  
259 ~~2010; Clavell and Berástegui, 1991; Maillard et al., 1992; Ribó et al., 2016b, 2016a;~~  
260 ~~Soler et al., 1983).~~ The Cenozoic succession starts with a transition from  
261 continental clastic sediments to marine platform carbonates, ending with a deposit  
262 formed by progradational terrigenous shelf-talus sediments ([Arche et al., 2010](#);  
263 [Clavell and Berástegui, 1991](#); [Etheve et al., 2018](#); [Lanaja, 1987](#); [Maillard et al., 1992](#);  
264 [Ribó et al., 2016b, 2016a](#); [Roca and Desegaulx, 1992](#); [Soler et al., 1986](#)).

265 The Neogene succession onshore of the southwestern Valencia Trough (Fig. 4)  
266 mostly consists of middle–late Miocene continental to marginal marine deposits,  
267 ~~including limestones, marls and coarse-grained detrital sediments.~~ ~~In the offshore~~  
268 ~~part of the study area, the Miocene stratigraphic succession is entirely marine. The~~  
269 ~~base of the Miocene sequence is composed of a basal conglomerate overlain by~~  
270 ~~coralline algal limestones. The middle Miocene (late Langhian–Serravallian) deep~~  
271 ~~marine calcareous claystones, marls and fine-grained sandstones overlie the algal~~  
272 ~~limestones or rest directly on deeply eroded Mesozoic rocks. Within the southern~~

273 ~~and central parts of the study area, the early-middle Miocene sequence is no more~~  
274 ~~than 200 m thick. Towards the north, the middle Miocene interval rapidly thickens,~~  
275 ~~reaching almost 2000 m. Tortonian and Messinian deposits consist of mainly marls~~  
276 ~~with thicknesses varying between 180 m and 425 m. The top of the Tortonian-~~  
277 ~~Messinian Miocene series is an erosional unconformity (Messinian Erosion Surface~~  
278 ~~(MES)) (Stampfli & Höcker, 1989; Lofi et al., 2011; Cameselle et al., 2014).~~

279 ~~In the onshore and nearshore areas, upper Miocene deposits are overlain by thin~~  
280 ~~cover (generally less than 50 m) of Pleistocene-recent alluvial fans, laterally grading~~  
281 ~~to lagoonal and beach barrier deposits near the coast. No Pliocene sediments have~~  
282 ~~been identified in the entire onshore coastal area, except for local karstic cave infills~~  
283 ~~with mammal remains (Agusti et al., 2011). Below the southern parts of the city of~~  
284 ~~Valencia, the thickness of Pleistocene-recent deposits abruptly increases. Vertical~~  
285 ~~electric sounding profiles seem to indicate the presence of several large normal~~  
286 ~~faults in this area, which have locally dropped the top Miocene surface down to~~  
287 ~~more than 400 m below sea level. From Cullera southwards, shallow boreholes~~  
288 ~~encounter Pleistocene to recent interbedded alluvial gravels, brackish lagoon, and~~  
289 ~~beach barrier deposits. Vertical electric sounding profiles and well correlations~~  
290 ~~indicate abrupt thickness changes, likely controlled by a complex system of normal~~  
291 ~~faults in the Mesozoic-middle Miocene basement, ranging from less than 50 m in~~  
292 ~~offset to more than 200 m towards the coast. Subsidence in the southern Valencian~~  
293 ~~coastal area continues to the present day, as evidenced by well-documented~~  
294 ~~submerged beach barriers of Tyrrhenian age (Eemian interglacial, 127-106ky),~~  
295 ~~which are currently found between 10 and 40 m below sea level in shallow offshore~~  
296 ~~areas (Zazo et al, 1979; Alcántara-Carrió et al, 2012).~~

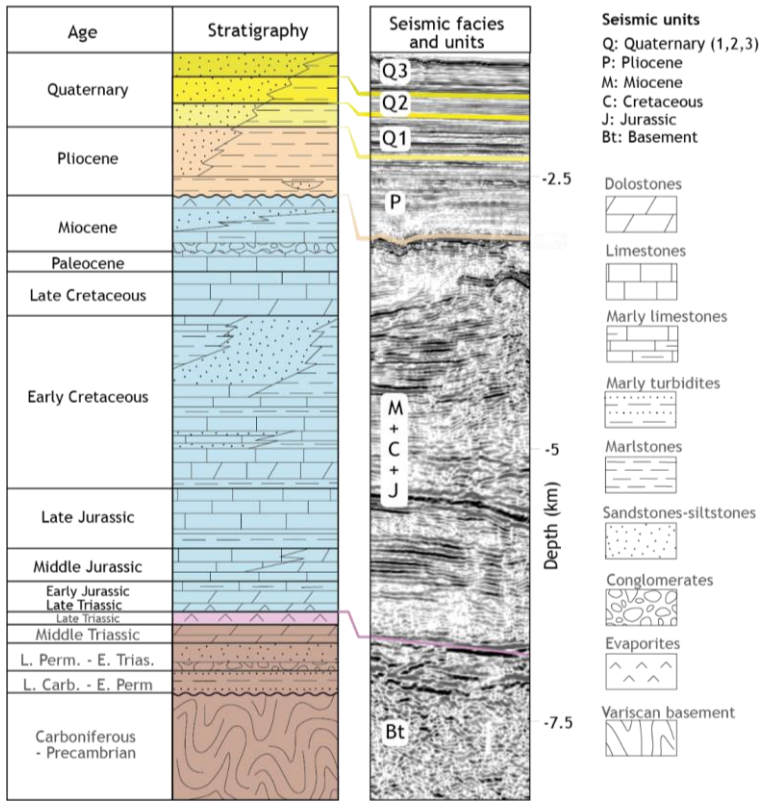
297 ~~In the offshore area,~~ Pliocene-recent sediments form a large prograding shelf  
298 complex with prominent clinofolds visible in seismic data, which downlap onto the  
299 MES. Prominent undulations on slope foresets are visible on most seismic lines and  
300 are interpreted as sediment waves (Ribó et al., 2015). In the offshore wells, the  
301 stratigraphic succession consists of an overall shallowing-upward series of thick  
302 grey claystones with calcareous interbeds at the base, grading upwards into  
303 sandstones and shell beds at the top. No unconformities have been identified in the

304 entire sequence, except for erosional gullies and canyons at the shelf edge. The Plio-  
305 Quaternary sequence reaches a maximum thickness of approximately 3000 m.

306 To determine the Plio-Quaternary depositional history and slip rate of major faults,  
307 six seismic horizons have been mapped and dated with palaeontological data from  
308 offshore wells, via the biostratigraphic scheme of Lirer et al. (2019). Starting from  
309 the Messinian unconformity at 5.3 Ma, seismic markers have been dated at 3.8 Ma  
310 (LO of *G. margaritae*), 3.3 Ma (FO *G. bononiensis*), 2.6 Ma (LCO *G. obliquus*) and 2.0  
311 Ma (FO *G. truncatulinooides*). As no samples were collected from any of the offshore  
312 wells above the lower-middle Pleistocene interval, an additional marker  
313 (approximately 1.0 Ma) ~~has been~~ was picked halfway through the 2.0 Ma marker and  
314 seabed (0 Ma), assuming a constant sedimentation rate.

315 Isopach maps (Fig. 5) were produced for the intervals of Pliocene (MES to 2.6 Ma  
316 marker) and Pleistocene–recent (2.6 Ma marker to the seabed), revealing a  
317 significant shift in the location of the depocentre. The Pliocene depocentre is  
318 located very close to the southern coast near Denia, attaining a maximum thickness  
319 of approximately 1500 m, whereas the Pleistocene depocentre has prograded ca.  
320 20 km to the NNW, reaching a thickness of more than 1750 m. The western  
321 shoreward edge of both the Pliocene and Pleistocene depocentres is controlled by  
322 very large NNW–SSE-trending normal faults (see below).

323 The described stratigraphic architecture indicates significant mechanical layering  
324 in the southwestern Valencia Trough. A rigid basement is overlain by a mechanically  
325 weak layer represented by the Upper Triassic Keuper Facies. Above this interval, a  
326 rigid Mesozoic carbonate succession is present, followed by a semirigid layer  
327 composed of primarily detrital deposits.



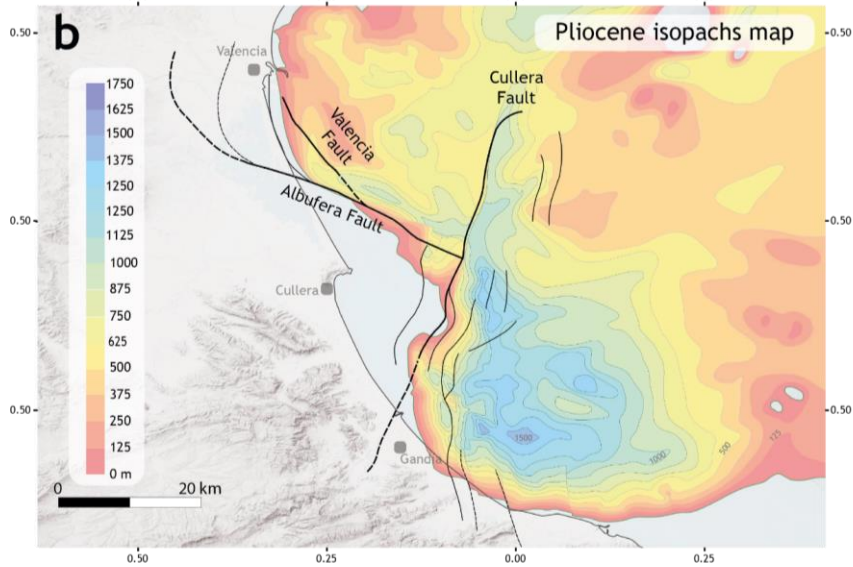
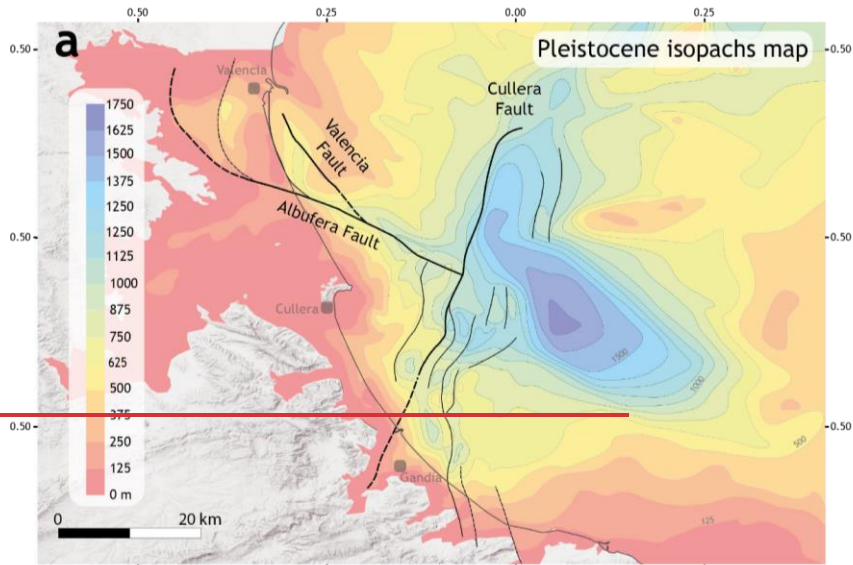
328

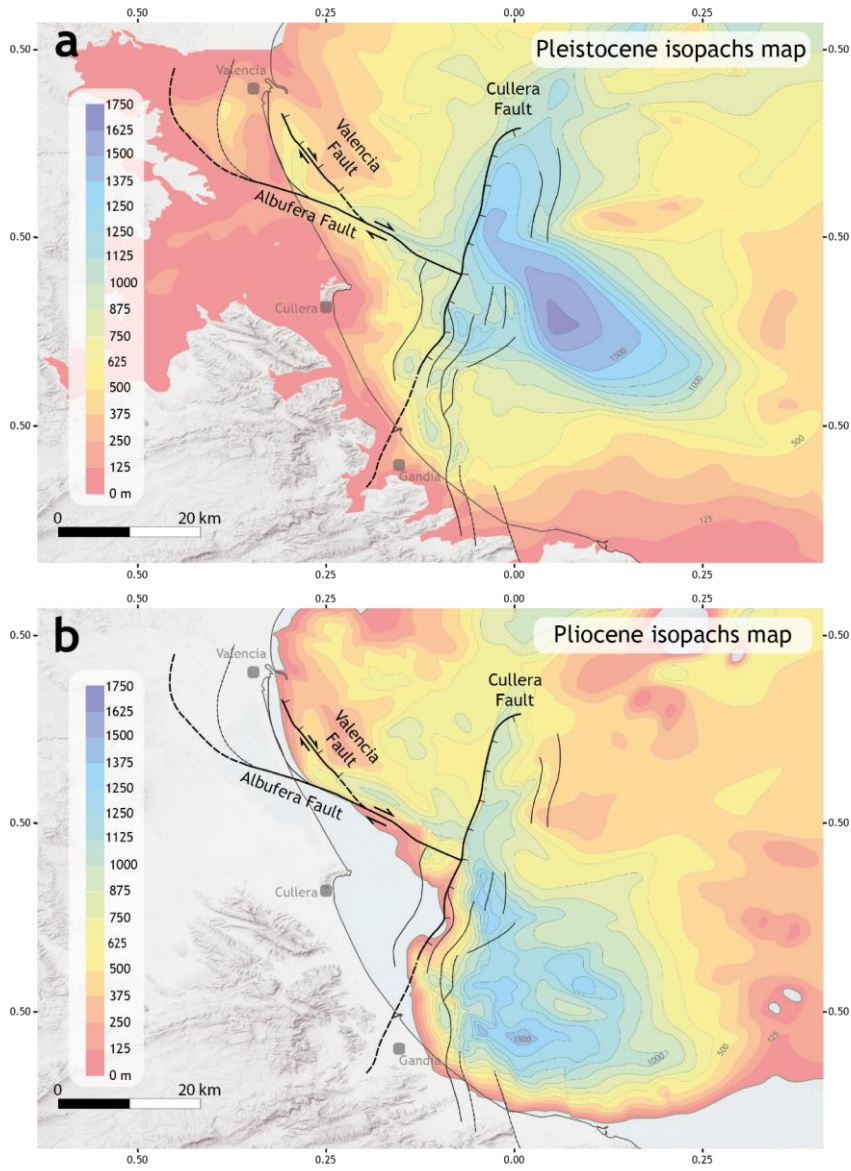
329

330

331

Figure 4: Chronostratigraphic diagram of the southwestern Valencia Trough. Note that the depth scale shows maximum thicknesses of the units.





333

334 Figure 5. Isopach maps of the southwestern Valencia Trough for the Pleistocene (a)  
 335 and Pliocene (b). The traces of the active faults are also depicted. Fault traces

336 represent the horizontal projection of the direction line of the fault plane, located  
337 midway between the intersection line of the top-of-the-Pliocene horizon and the  
338 top-of-the-Quaternary horizon. Fault traces are derived primarily from their position  
339 on seismic profiles, supplemented by isopach maps and observed thickness  
340 variations in stratigraphic units, as indicated by the available wells. Dashed lines  
341 show interpreted traces. Modified from Ramos et al. (2025).

342 **5. Main active faults in the southwestern Valencia Trough**

343 In this section, we describe the main structural features of the southwestern  
344 Valencia Trough after the analysis of gravity data and isopach maps obtained from  
345 the subsurface dataset (seismic lines, wells and VES) (Figs. 3 and 5).

346 The filtered Bouguer anomaly map (Fig. 3) reveals a positive anomaly in the central  
347 part of the study area, referred to as the Cullera anomaly. This positive anomaly is  
348 surrounded by a region exhibiting a negative anomaly, particularly in the offshore  
349 area located east of Cullera. We interpret this pattern of **anomaly anomalies** to be  
350 because of mass excess associated with a basement high (Cullera positive  
351 anomaly) surrounded by a region with greater sedimentary cover (negative  
352 anomaly). This interpretation is further supported by the isopach maps derived from  
353 interpretation of the subsurface data (Fig. 5). The negative gravity anomaly  
354 correlates with an abrupt increase in the thickness of both the Pliocene and  
355 Quaternary sedimentary successions. Furthermore, the transitions in both the  
356 gravity anomaly and sedimentary thickness correspond to the positions of the main  
357 faults observed in the seismic dataset (see below). On the basis of this evidence, we  
358 propose that the southwestern Valencia Trough is structurally characterised by the  
359 presence of three major faults offsetting the basement and significantly influencing  
360 the stratigraphic evolution of the area. These three major faults are: the Cullera  
361 Fault, the Valencia Fault and the Albufera Fault (Fig. 5).

362 The structural configuration of the southwestern Valencia Trough is also influenced  
363 by the presence of Upper Triassic evaporites and shales at the base of the Mesozoic  
364 sedimentary cover. **Major faults offsetting the Mesozoic-Quaternary succession**  
365 **present a listric geometry with a main ramp that flattens out in the Upper Triassic**  
366 **salt layer (Fig. 6). These geometries have been interpreted as evidence of a strain**  
367 **partitioning between the suprasalt and the subsalt successions** (Etheve et al., 2016;  
368 Fang et al., 2021; Muñoz Martín & Vicente Muñoz, 1988). **According to these**  
369 **interpretations, the Upper Triassic is a This**-mechanically weak layer **that** induces  
370 tectonic decoupling within the seismogenic crust of the southwestern Valencia  
371 Trough. As a result, the deformation style of the suprasalt succession (cover) differs  
372 significantly from that of the subsalt succession (basement) (Etheve et al., 2018;

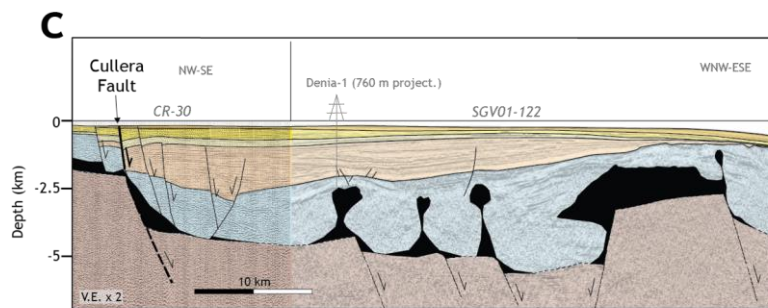
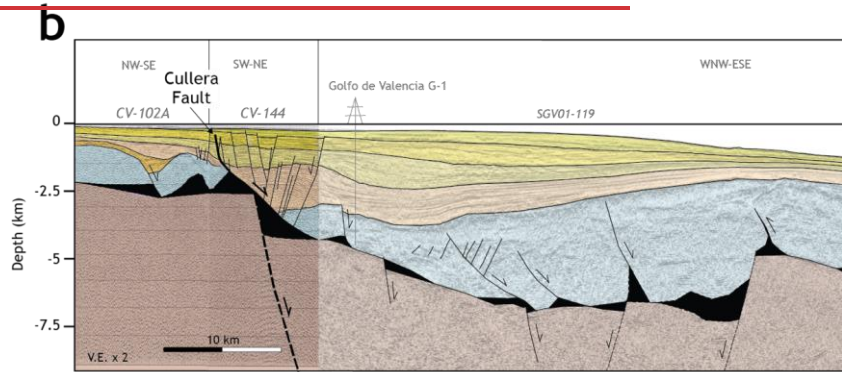
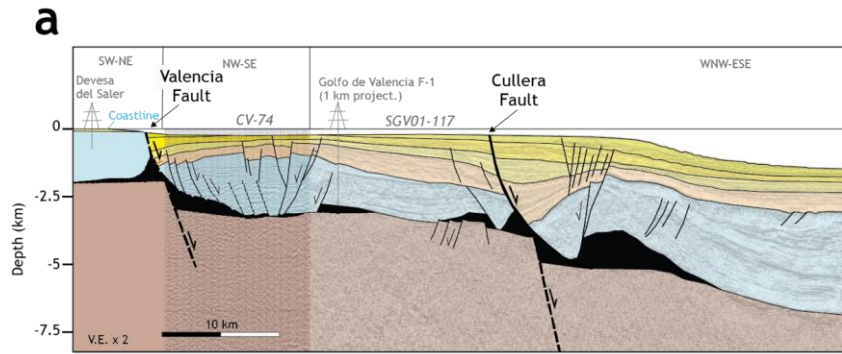
Con formato: Inglés (Estados Unidos)

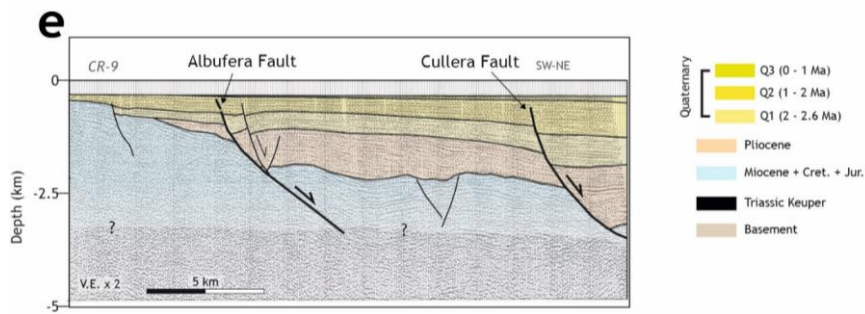
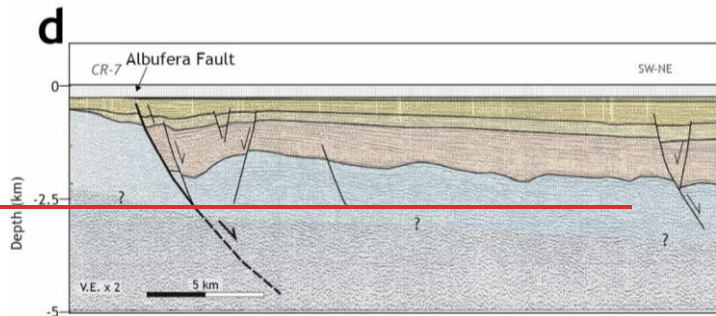
Con formato: Inglés (Estados Unidos)

373 Fang et al., 2021; Ramos et al., 2023, 2025; Roma et al., 2018). The main difference  
374 is that normal faults present a listric geometry in the cover, while these faults are  
375 planar within the basement (see below).

376 The analysis of the seismic reflection profiles (Fig. 6) reveals three ~~distinct~~ fault  
377 types: i) faults restricted to the subsalt basement; ii) faults restricted to the  
378 suprasalt cover; and iii) faults cutting through the sedimentary cover, basement and  
379 salt layer.

380



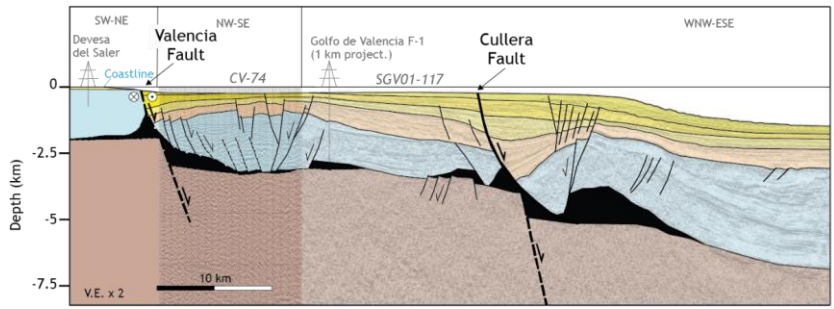


382

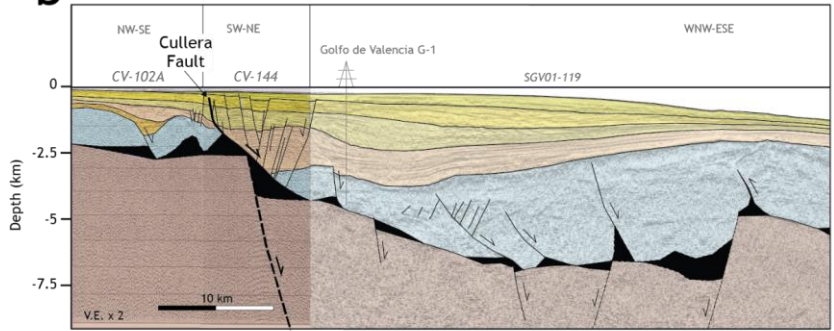
383

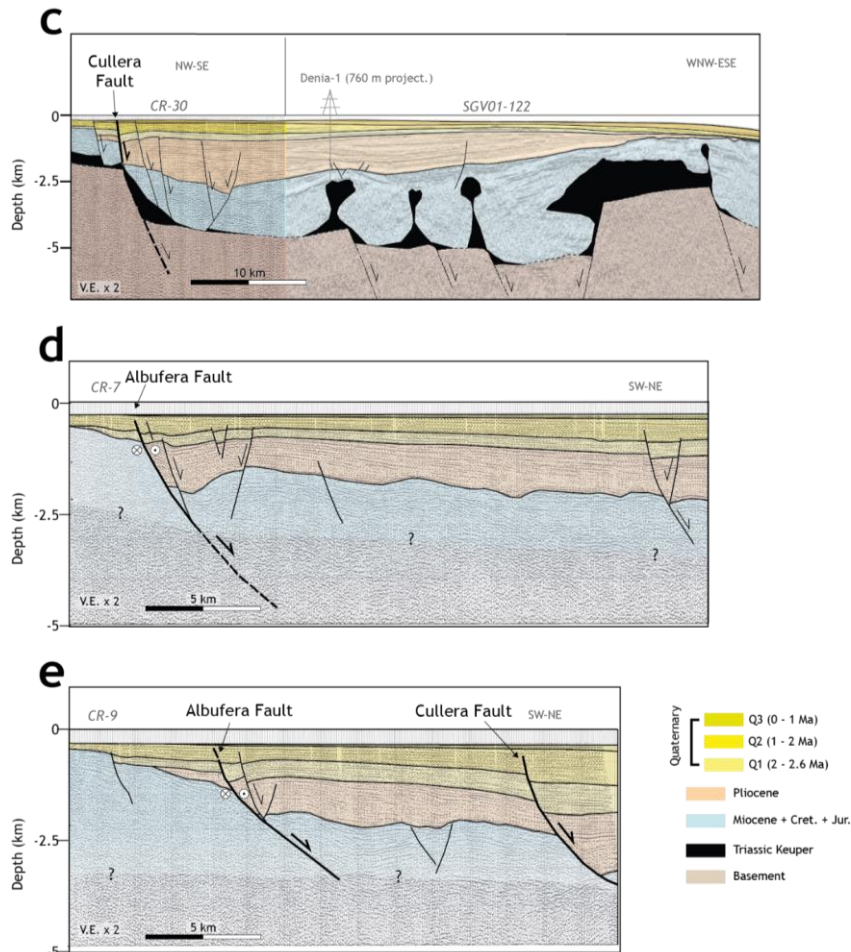
384

**a**



**b**





386  
 387 Fig. 6. Interpreted sections derived from onshore cross-sections (a) and the offshore  
 388 2D seismic profiles (a-e). Sections in a-d depict the structure of both the supra- and  
 389 subsalt successions, while in sections in d-e only the suprasalt structure is  
 390 represented. See Fig. 3 for the location. a-c sections after Ramos et al., 2025. Unit  
 391 colours are as those in Fig. 4 (except for the Triassic unit). Note the x2 vertical  
 392 exaggeration of all the sections.

393

394 **5.1 Cullera Fault**

395 The Cullera Fault is the longest along-strike fault in the region, spans approximately  
396 59 km, and has the highest cumulative offset, with more than 1800 m of vertical  
397 displacement at the top of the Messinian horizon (Figs. 5 and 6).

398 The along-section geometry of the fault across the suprasalt succession is well  
399 imaged in the seismic reflection dataset (Fig. 6). The Cullera Fault is a normal, NNE–  
400 SSW-trending fault that dips highly towards the east. The fault offsets the entire  
401 suprasalt cover, including the 1 Ma horizon. Owing to the low resolution of the  
402 available bathymetric data, it is not possible to confirm whether the fault offsets the  
403 seafloor. The Cullera Fault displaces the top of the basement horizon, indicating  
404 that this fault involves both subsalt and suprasalt successions.

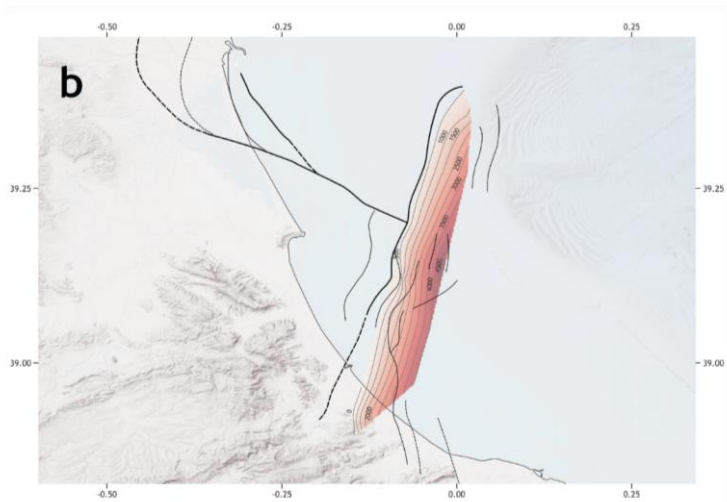
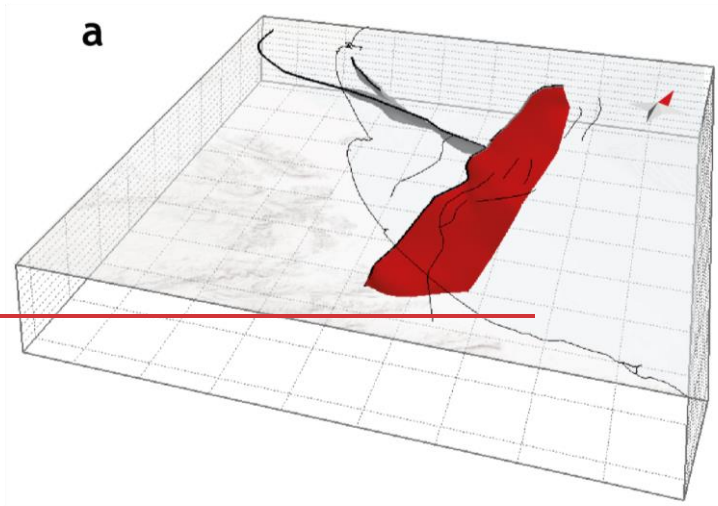
405 Within the basement, the Cullera Fault is poorly imaged in seismic profiles.  
406 Nevertheless, the available data suggest that it is a planar fault (Fig. 6). This is also  
407 supported by the absence of significant tilting of the basement-top horizon.

408 In contrast, the geometry of the Cullera Fault in the sedimentary cover is  
409 heterogeneous. In the northern area (Fig. 6), the part of the Cullera Fault offsetting  
410 the cover exhibits a listric geometry, which is responsible for the development of a  
411 rollover structure in the hanging wall (Fig. 6). ~~This listric geometry consists of a highly  
412 dipping (50–60°) upper part offsetting the Plio-Quaternary succession and a gently  
413 dipping (20–30°) lower part in the Mesozoic cover.~~ Southwards, the listric geometry  
414 and related rollover fold becomes less pronounced (Fig. 6).

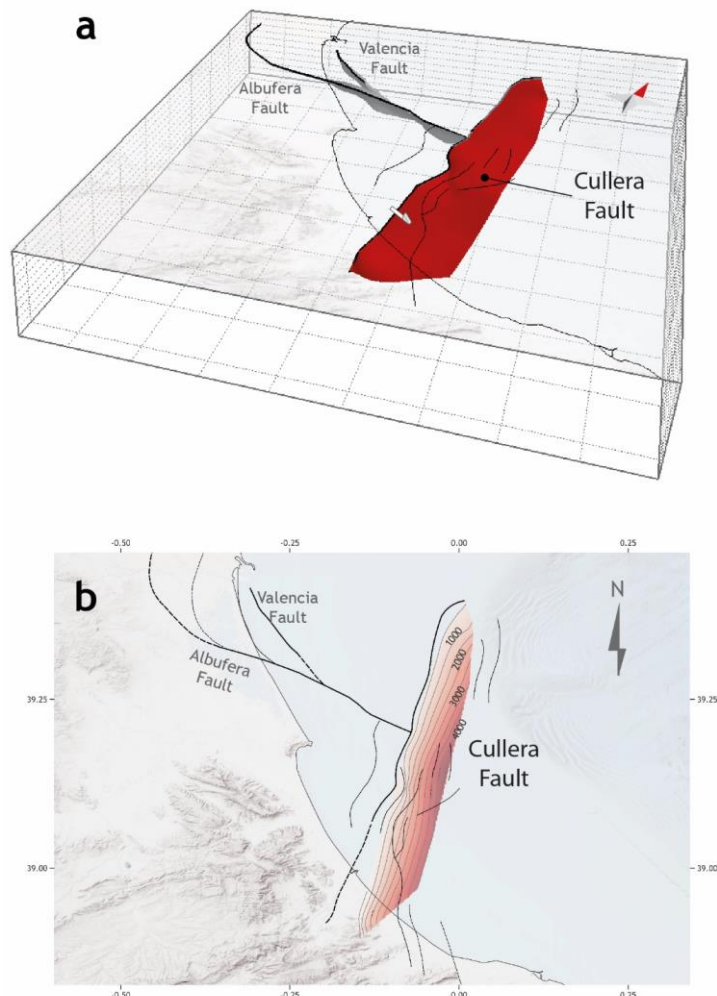
415 To better constrain the geometry of the Cullera Fault, we constructed a structural  
416 map of the fault by integrating fault traces identified in the seismic reflection dataset  
417 with isopach maps (Fig. 7). Additionally, a 3D model of the Cullera Fault, along with  
418 the two other major faults, was generated following a 2½D construction approach,  
419 integrating interpreted seismic profiles via interpolation. We employed the ordinary  
420 kriging algorithm implemented in MOVE software, a methodology consistent with  
421 previous approaches applied to analogous structures (Ramos et al., 2020), ~~ensuring  
422 a geologically consistent representation of the fault geometry in the subsurface.  
423 This approach allows for the reconstruction of complex fault surfaces by integrating  
424 available geophysical data while minimising spatial uncertainties.~~ Analysis of the

425 reconstructed 3D fault indicates that the surface area of the Cullera Fault offsetting  
426 the sedimentary cover is approximately 360 km<sup>2</sup>.

427



428



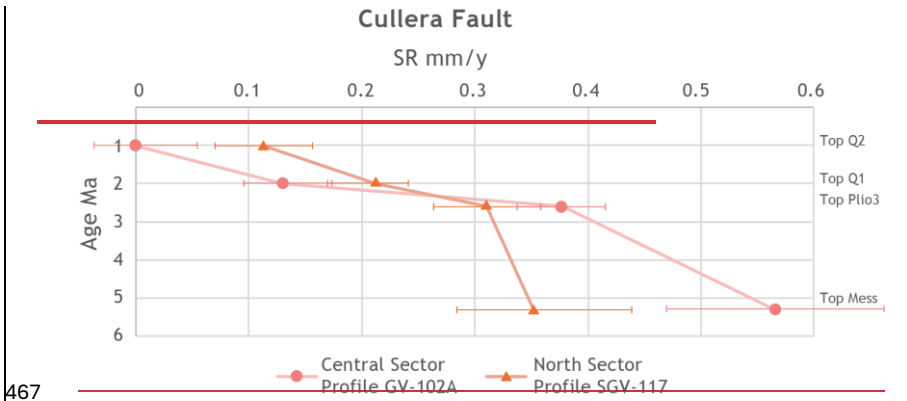
429  
 430 Figure 7. 3D model (a) and structural map (b) of the Cullera Fault (red surface).  
 431 Squares in figure 7a represent 10 km x 10 km. Note the red arrow pointing to the  
 432 North-north in figure 7a.

433

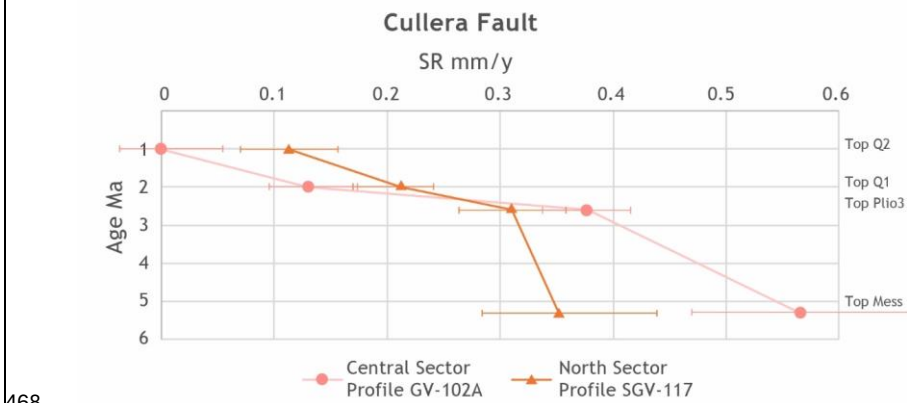
434 Several minor normal faults have developed in the hanging wall of the Cullera Fault  
 435 (Figs. 5). These faults displace only the suprasalt succession without affecting the  
 436 underlying subsalt units. In previous studies (e.g., Perea 2006; Roca 1992), distinct  
 437 names were assigned to these faults, such as the Western Cabo Cullera Fault,

438 Central Cabo Cullera Fault, and Eastern Cabo Cullera Fault. However, the improved  
439 resolution and quality of the new seismic dataset enable a more detailed  
440 characterisation of these tectonic structures, allowing for a reassessment of their  
441 nomenclature and role. ~~On the basis of our analysis, we~~We interpret these minor  
442 faults to be part of the damage zone associated with the main Cullera Fault. ~~Fault~~  
443 ~~damage zones typically consist of subsidiary structures that develop in response to~~  
444 ~~the distribution of strain surrounding a major fault. In this context, these minor faults~~  
445 ~~represent secondary features that contribute to the overall deformation but are~~  
446 ~~structurally subordinate to the Cullera Fault. Consequently, we propose~~  
447 ~~consolidating the nomenclature to avoid potential confusion. Instead of assigning~~  
448 ~~separate names to these subsidiary faults, we retain the term Cullera Fault~~  
449 ~~exclusively for the main structure.~~

450 The quality of the seismic dataset ~~in profiles GV-102A and SGV-117 (Fig. 3)~~ allows for  
451 an analysis of the slip rate of the Cullera Fault. This analysis is approximate,  
452 because of the resolution of the seismic profiles, the uncertainties in the recognition  
453 of the markers in the hanging wall and footwall, and the age of these markers. Net  
454 slip rates were obtained for the Top-Messinian, Top Pliocene, Top-Q1, and Top-Q2  
455 horizons, with assigned ages of 5.3 Ma, 2.6 Ma, 2 Ma, and 1 Ma, respectively.  
456 ~~Analogous values of the slip rate for each of these markers were obtained from the~~  
457 ~~two analysed seismic profiles.~~ (Fig. 8). The slip rates for the Cullera Fault seem to  
458 have decreased over time, as the calculation yielded mean slip rates of  $0.40 \pm 0.1$   
459 mm/y for the Pliocene and  $0.15 \pm 0.1$  mm/y for the Quaternary. ~~This slip rate~~  
460 ~~reduction could be the consequence of a change in the regional tectonic regime in~~  
461 ~~the complex tectonic cadre of the western Mediterranean region. However, as the~~  
462 ~~Cullera Fault is a salt-influenced structure, different mechanisms control fault~~  
463 ~~offset. We discuss in section 6 the potential reasons behind this observed decrease~~  
464 ~~in slip rate. In any case~~However, we cannot dismiss that ~~at least part of~~ this apparent  
465 in-time evolution could be an artefact related to the epistemic uncertainties  
466 mentioned above.



467



468

469 Figure 8. Long term slip rates (SR) for the Cullera Fault derived from the seismic  
 470 profiles for the Top Messinian, Top Plio3, Top Q1, and Top Q2 horizons. ~~Pink~~The pink  
 471 line and dots represent SR for the central sector of the fault. ~~Orange~~The orange line  
 472 and triangles indicate SR for the north sector of the fault. ~~Slip~~The slip rates seem to  
 473 decrease in time, from  $0.40 \pm 0.1$  mm/y for the Pliocene to  $0.15 \pm 0.1$  mm/y for the  
 474 Quaternary. Error bars are estimated on the basis of uncertainties in the recognition  
 475 of the markers and their ages.

476

477 **5.2. Albufera Fault**

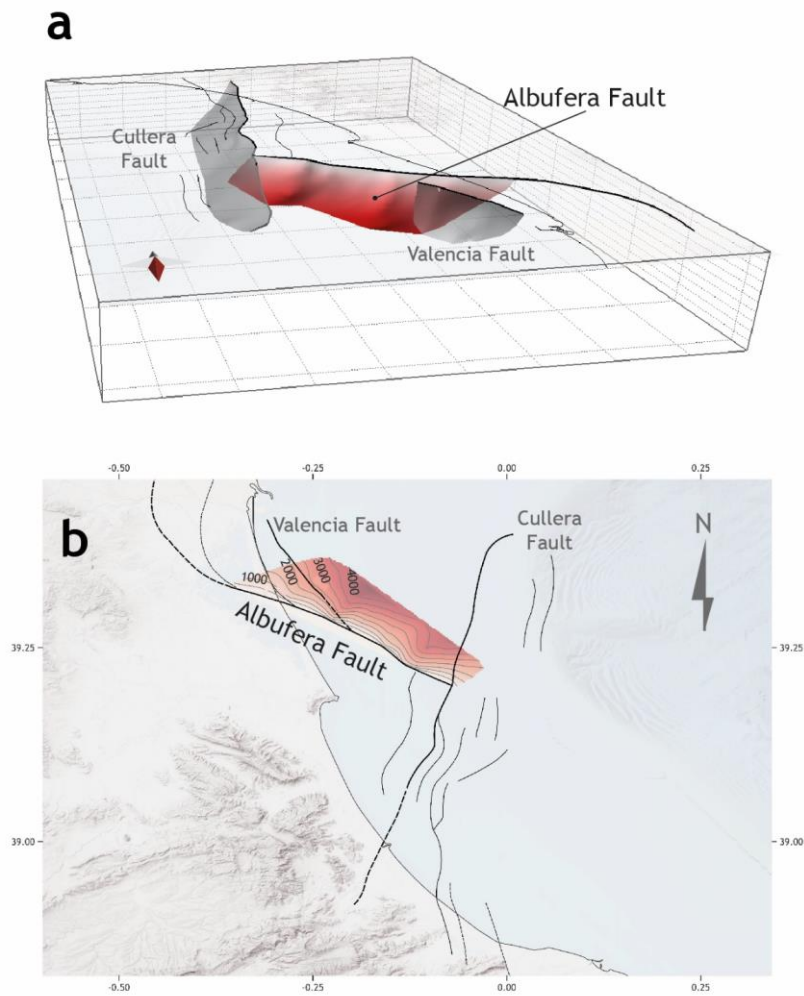
478 The Albufera Fault (~~F3~~) (Figs. 5 and 6) is a newly defined active structure in the  
 479 southwestern Valencia Trough. This NW–SE striking fault extends approximately 55

480 km and ~~presents an oblique kinematic, with a major strike slip component and a~~  
481 ~~minor normal displacement (see below). The Albufera Fault~~ exhibits a maximum  
482 ~~normal-vertical~~ offset of 1000 m for the Top-Messinian horizon. This would imply a  
483 long-term ~~vertical~~ slip rate of  $0.2 \pm 0.1$  mm/y. The fault offsets both the supra- and  
484 subsalt successions (Figs. 5 and 6). The Albufera Fault is visible only in the vintage  
485 seismic reflection dataset, where it presents a low dip and a listric geometry.

486 The Albufera Fault appears to offset the entire suprasalt cover, including the 1 Ma  
487 horizon. As with other faults in the region, the low resolution of the available  
488 bathymetric data prevents us from determining whether this fault offsets the  
489 seabed. Nevertheless, high-resolution seismic profiles from the offshore shelf  
490 analysed by previous authors indicate seabed offsets caused by secondary normal  
491 faults likely associated with the Albufera Fault (Díaz de Ríó et al., 1986; Albarracín  
492 et al., 2013).

493 The available seismic dataset reveals a normal kinematic component for the  
494 Albufera Fault. However, mapping of small-scale fault traces in upper Pleistocene–  
495 recent sediments (interval between the seabed and the 1.8 Ma horizon) reveals that  
496 these faults are oblique to the main trend of the Albufera Fault, forming an en  
497 echelon pattern in map view, which suggests that the Plio-Quaternary reactivation  
498 of the main fault has a significant right-lateral strike-slip component. This dextral  
499 component ~~along the NW-SE trending fault~~ is consistent with the regional ENE–  
500 WSW direction of Plio-Quaternary extension in the southwestern Valencia Trough  
501 and kinematically consistent with NNW–SSE trending normal faults. The fault  
502 influences the Plio-Quaternary sedimentary infill of the southwestern Valencia  
503 Trough (Fig. 5). The ~~computed~~ isopach maps reveal that the Pliocene ~~and~~  
504 ~~Quaternary~~ succession significantly increased in the hanging wall relative to the  
505 footwall. ~~Similarly, the Quaternary succession is thicker in the hanging wall than in~~  
506 ~~the footwall.~~–The listric geometry of the Albufera Fault is responsible for the  
507 development of a rollover anticline in the hanging wall (Fig. 6). This anticline is likely  
508 accentuated by the palaeoshelf edge of the late Tortonian–early Messinian shelf,  
509 which is located in the central part of the rollover structure.

510 To further constrain the geometry of the Albufera Fault, a structural map [and a 3D](#)  
511 [model](#) of the fault was constructed (Fig. 9). Analysis of the reconstructed 3D fault  
512 surface indicates that the fault encompasses an area of approximately 560 km<sup>2</sup>.



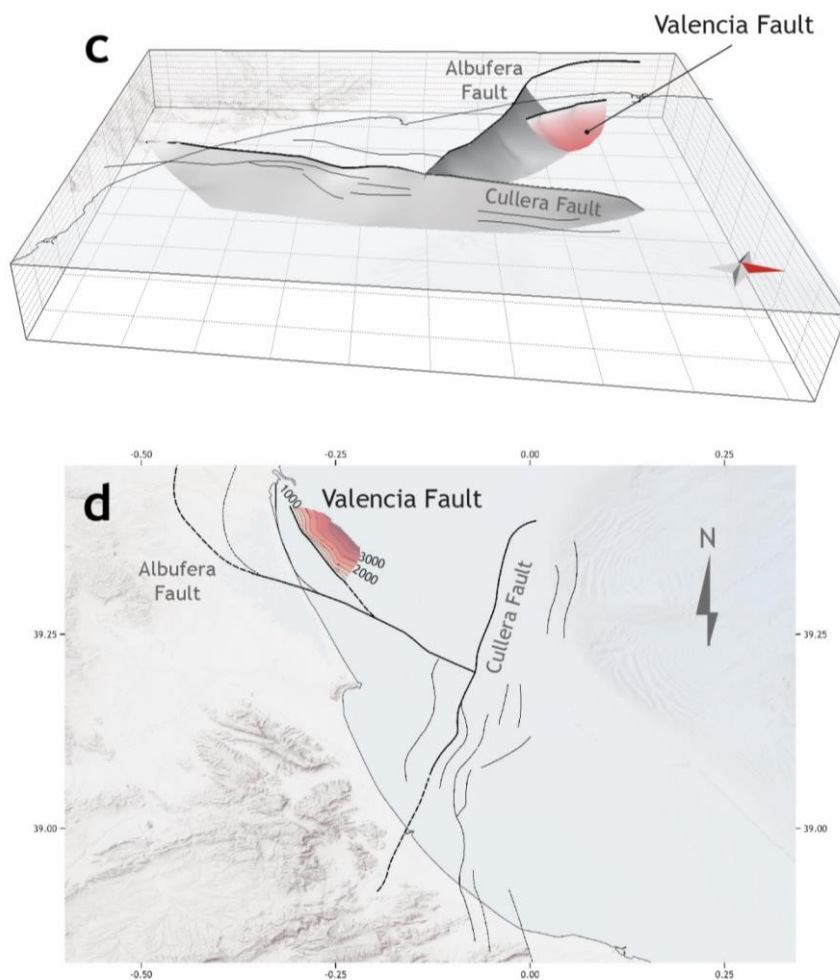
513

514

515

516

517



518

519 Figure 9. 3D model and structural map of the Albufera Fault (a and b) and the  
 520 Valencia Fault (c and d). Squares in the 3D models represent 10 km x 10 km boxes.  
 521 Note the red arrow pointing to the North-north in figures 9a and 9c.

522

523

524 **5.3 Valencia Fault**

525 In this section, we ~~define for the first time describe~~ the Valencia Fault (Figs. 5 and 6).  
526 ~~This structure could correspond to the Western Cabo Cullera Fault (sensu Perea,~~  
527 ~~2006). The Valencia Fault presents a~~~~This structure is considered one of the main~~  
528 ~~active faults in the southwestern Valencia Trough because of its~~ length of  
529 approximately 20 km and ~~its~~~~has a~~ significant impact on the distribution of  
530 Quaternary depocentres. The Valencia Fault ~~present a normal component, as it~~  
531 ~~vertically~~ displaces both the supra- and subsalt successions (see below) (Figs. 5  
532 and 6). ~~However, taking into account the general structural arrangement of the~~  
533 ~~southwestern Valencia Trough, we postulate that the Valencia Fault presents also a~~  
534 ~~strike-slip component.~~

535 This NNW–SSE trending, steeply dipping fault is imaged primarily in the vintage  
536 seismic reflection dataset, where it exhibits a listric geometry, at least in the portion  
537 offsetting the suprasalt succession (Fig. 6). The Valencia Fault ~~vertically~~ offsets the  
538 entire suprasalt cover, including the 1 Ma horizon. However, owing to the low  
539 resolution of the available bathymetric data, it is not possible to determine whether  
540 this fault offsets the seabed. The Valencia Fault also displaces ~~vertically~~ the top of  
541 the basement horizon, indicating that this structure involves both subsalt and  
542 suprasalt successions. Within the basement, the Valencia Fault is not well-imaged  
543 in the seismic profiles, but the absence of tilting in the basement-top horizon  
544 suggests that it is a planar fault (Fig. 6). The Valencia Fault and its secondary strands  
545 very likely continue onshore below the City of Valencia. The lack of onshore seismic  
546 data hampers the mapping of these fault strands, but their presence can be inferred  
547 from the abrupt Plio-Quaternary thickness changes observed in water wells and  
548 ~~Vertical-vertical e~~Electric ~~Sounding-sounding~~ profiles.

549 To further constrain the geometry of the Valencia Fault, a structural map ~~and a 3D~~  
550 ~~model~~ of the fault was constructed (Fig. 9). Analysis of the reconstructed 3D fault  
551 surface indicates that the fault encompasses an area of approximately 208 km<sup>2</sup>.

552

553 **6. Evolutionary growth of the Cullera Fault: interplay between tectonics and**  
554 **salt withdrawal.**

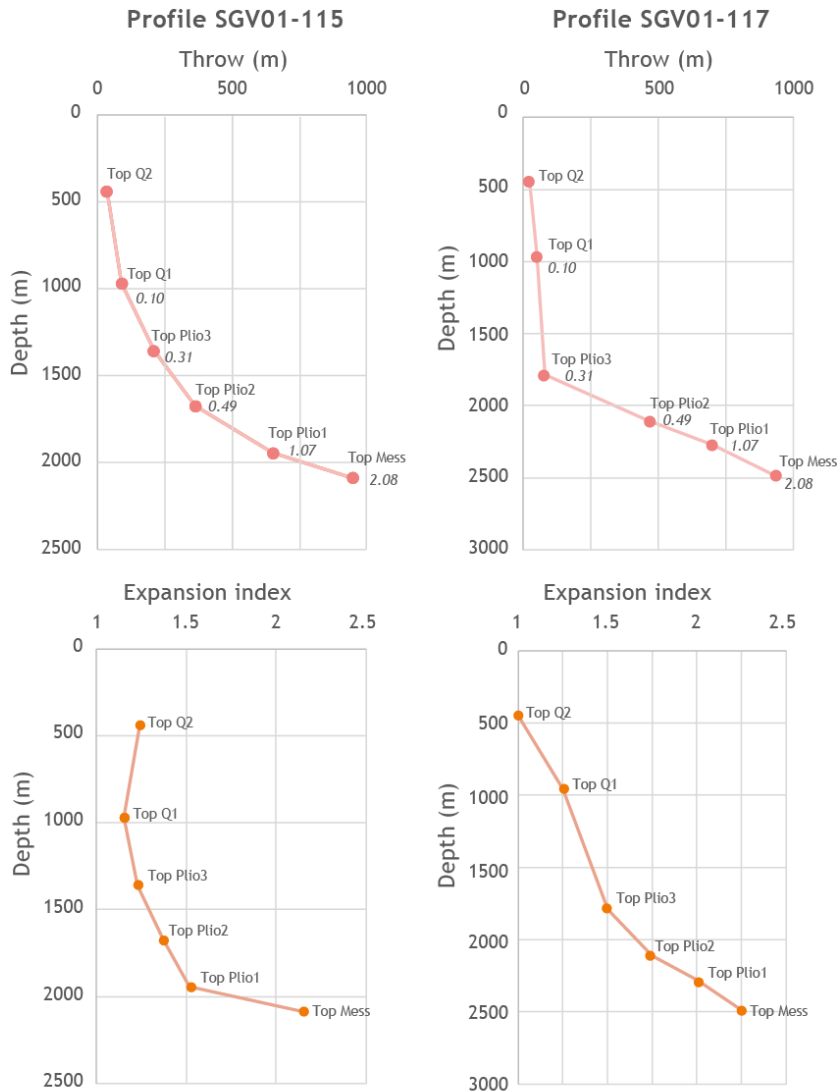
Con formato: Interlineado: 1.5 líneas

555 This section aims to provide further insights into the evolution of the active faults in  
556 the southwestern Valencia Trough. The low resolution of the vintage seismic dataset  
557 limits the ability to perform a detailed analysis only for the Cullera Fault. To analyse  
558 recent along-dip variations in throw, we constructed throw-depth plots (T-z plots)  
559 for the post-Messinian markers (Fig. 10). These plots provide insights into the  
560 evolutionary growth of the fault (Mansfield and Cartwright, 1996; Hongxing and  
561 Anderson, 2007). The quality of the available seismic reflection dataset allows this  
562 analysis to be performed on two seismic profiles located in the northern part of the  
563 fault, where the listric geometry is well-developed (LINES SGV01-115 and SGV01-  
564 117; Figs. 3 and 6).

565 We computed T-z plots for six suprasalt horizons: Top-Messinian, Top Plio1, Top  
566 Plio2, Top Plio3, Top Q1, and Top Q2 (Fig. 10). The T-z plots for the Cullera Fault reveal  
567 a general increase in the throw and throw gradient with depth. ~~We postulate that the~~  
568 ~~increase observed in the throw is the result the differing ages of the horizons, older~~  
569 ~~horizons show greater offset because they have been displaced over a longer time~~  
570 ~~interval. However~~As regards throw gradients, the data indicate two distinct portions  
571 ~~with differing throw gradients~~: (i) the lower portion, with higher throw gradients,  
572 includes horizons from the Top Messinian to the Top Pliocene; (ii) the upper portion,  
573 with lower throw gradients, comprises the Quaternary horizons. This distinction  
574 ~~between these two portions~~ is particularly pronounced in the southern seismic line  
575 (line SGV01-117, Fig. 6). Here, the throw gradient decreases, from 2.38 ~~-~~2.98 in the  
576 lower portion to 0.22 ~~-~~0.10 in the upper portion.

Con formato: Inglés (Estados Unidos)

Con formato: Inglés (Estados Unidos)



577

578 Figure 10. Throw depth (T-z) and expansion index plots for the Cullera Fault  
 579 computed from profiles SGV01-115 and SGV01-117. The numbers within the T-z  
 580 plots indicate the throw gradient for the corresponding interval. The T-z plots reveal  
 581 an increase in the throw and throw gradient, with a higher throw gradient for the Top  
 582 Messinian–Top Pliocene interval and a lower throw gradient for the Quaternary  
 583 interval.

584 The Cullera Fault significantly influences the Plio-Quaternary sedimentary infill of  
585 the southwestern Valencia Trough. Isopach maps indicate a marked increase in the  
586 thickness of both Pliocene and Quaternary successions in the hanging wall with  
587 respect to the footwall (Fig. 5). ~~This thickness variation offers critical insights into~~  
588 ~~the history of fault growth.~~ To quantify this relationship, we computed the expansion  
589 index (Thorsen, 1963; Rouby et al., 2003; Jackson and Rotevatn, 2013) for the post-  
590 Messinian stratigraphic units (Fig. 10). The expansion index consistently exceeds 1  
591 across all the analysed intervals, indicating a synkinematic deposition in these  
592 units. ~~Notably, the~~ ~~The~~ Pliocene units exhibit a greater expansion index than the  
593 Quaternary units do, with the difference being particularly pronounced in the  
594 southern seismic line (Fig. 6 LINE SGV01-117).

595 Finally, to shed light on the mechanisms controlling the creation of accommodation  
596 space related to the Cullera Fault, we analyse the tectonic-stratigraphic  
597 arrangement of the hanging wall units. ~~To discuss this point, we compare the~~  
598 ~~geometries observed in the southwestern Valencia Trough with analogous~~  
599 ~~stratigraphic geometries in the Danish North Sea, where they have been interpreted~~  
600 ~~in terms of the evolution of salt-influenced faults (Duffy et al., 2023 and references~~  
601 ~~therein). In such a setting, two mechanisms create accommodation space: fault~~  
602 ~~displacement and load-driven salt withdrawal in the hanging-wall. These two~~  
603 ~~mechanisms can act separately or contemporaneously in time. When the~~  
604 ~~accommodation space generated by the fault offset exceeds that created by salt~~  
605 ~~withdrawal, the depocentre axis remains adjacent to the fault. In contrast, when~~  
606 ~~salt-related accommodation space is dominant, the depocentre migrates away~~  
607 ~~from the fault (Duffy et al., 2023).~~

608 In the northern part of the Cullera Fault, where the rollover structure is well  
609 developed (Fig. 6), the position of the Plio-Quaternary depocentre in the hanging-  
610 wall varies along the dip direction. The Pliocene depocentre remains in the  
611 immediate hanging wall of the fault. ~~Therefore, we interpret that, during the~~  
612 ~~Pliocene, the accommodation space generated by the displacement of the Cullera~~  
613 ~~Fault exceeded that produced by the accommodation space related to salt~~  
614 ~~withdrawal. However,~~ ~~d~~ During the deposition of unit Q1, the depocentre migrated

Con formato: Inglés (Estados Unidos)

615 basinwards, suggesting that salt withdrawal-related accommodation space  
616 outpaced that related to fault displacement. Finally, during Q2 and Q3, the  
617 depocentre axis shifted towards the fault, indicating that fault displacement-related  
618 accommodation space regained dominance over salt mobility.

619 The depocentre of unit Q2 is located adjacent to the fault, whereas the depocentre  
620 of unit Q3 is located further east, related to the progradational geometry of the  
621 sedimentary bodies. Nevertheless, when focusing strictly on the area affected by  
622 the fault, the local Q3 depocentre also remains adjacent to the fault.

623 We postulate that this evolution in the location of depocentres is related to the  
624 mechanisms responsible for the creation of accommodation space. Analogous  
625 stratigraphic geometries have been observed in the Danish North Sea, where they  
626 have been interpreted in terms of the evolution of a salt-influenced fault (Duffy et  
627 al., 2023 and references therein). In such a setting, two mechanisms create  
628 accommodation space: fault displacement and load-driven salt withdrawal in the  
629 hanging-wall. These two mechanisms can act separately or contemporaneously in  
630 time. When the accommodation space generated by the fault offset exceeds that  
631 created by salt withdrawal, the depocentre axis remains adjacent to the fault. In  
632 contrast, when salt-related accommodation space is dominant, the depocentre  
633 migrates away from the fault (Duffy et al., 2023):

634 Accordingly, we interpret that, during the Pliocene, the accommodation space  
635 generated by the displacement of the Cullera Fault exceeded that produced by the  
636 accommodation space related to salt withdrawal, as evidenced by the depocentre's  
637 axis being located adjacent to the fault (Fig. 6). During the deposition of unit Q1, the  
638 depocentre migrated basinwards, suggesting that salt withdrawal-related  
639 accommodation space outpaced that related to fault displacement. Finally, during  
640 Q2 and Q3, the depocentre axis shifted towards the fault, indicating that fault  
641 displacement-related accommodation space regained dominance over salt  
642 mobility:

643 All the above-described features shed light on the evolution of the salt-influenced  
644 Cullera Fault. As previously discussed, the creation of accommodation space

645 results from two mechanisms: tectonic offset along the fault and displacement  
646 related to salt withdrawal. Both mechanisms act cumulatively; that is, both  
647 mechanisms produce slip along the Cullera Fault and create accommodation  
648 space. The migration of successive depocentres suggests that, during the Pliocene,  
649 accommodation space related to tectonic offset was greater than that created by  
650 salt withdrawal. As the throw gradient is high ( $\approx 2.4$ ) during this period, we postulate  
651 that both mechanisms were active. During the deposition of Q1 (2.6–2 Ma), the  
652 position of the depocentre suggests that salt mobility became the dominant  
653 mechanism, likely due to a decrease in fault activity, an increase in salt withdrawal,  
654 or both. As the throw gradient decreases during this period, we postulate that a  
655 decrease in the fault displacement rate could be the reason for the change in the  
656 main mechanism. Finally, during the rest of the Quaternary (2 Ma to present), fault  
657 displacement-related accommodation space once again exceeded that created by  
658 salt withdrawal. The constant throw gradient observed during this period with  
659 respect to the previous time interval (2.6–2 Ma) suggests that the change in the main  
660 mechanism was due to a reduction in or cessation of salt withdrawal. This  
661 interpretation is further supported by the off-fault geometry of the Q2–Q3  
662 sedimentary bodies, as no significant change in thickness is observed above the salt  
663 withdrawal-related anticlinal crest located east of the Cullera Fault (Fig. 6).

664 Therefore, according to the above exposed, we postulate that, during the Pliocene  
665 and lower Quaternary (up to 2 Ma ago), the offset of the Cullera Fault was produced  
666 by both tectonics and salt withdrawal, being the first mechanism dominant during  
667 the Pliocene and the second during the 2.6–2 Ma time span. From that moment to  
668 the present salt withdrawal ceases (or significantly reduces), and tectonics  
669 becomes the only (or very dominant) process~~the evolution of the Cullera Fault~~  
670 ~~during the Pliocene–Quaternary time span was controlled mainly by the tectonic~~  
671 ~~offset, except for the time interval between 2.6 and 2 Ma, when offset was related~~  
672 ~~mainly to salt withdrawal. The reduction of salt movement is possibly due to the~~  
673 ~~complete withdrawal of mobile salt and the formation of a weld below the hanging~~  
674 ~~wall. This evolution could also explain the slip rate decreases observed for the~~  
675 ~~Cullera Fault (Fig. 8). A higher slip rate is expected during the Pliocene, when both~~

Con formato: Inglés (Estados Unidos)

676 tectonics and salt withdrawal were active. Once salt withdrawal ceases or  
677 significantly decreases, a corresponding decrease in the slip rate is also expected.  
678

679 **7. Influence of mechanical layering on the seismic potential: the case of the**  
680 **southwestern Valencia Trough**

681 The southwestern Valencia Trough has a distinct mechanical stratigraphy  
682 characterised by ~~three layers: a subsalt basement, a weak mechanical layer~~  
683 ~~composed of Triassic evaporites, and a suprasalt overlain~~ Mesozoic–Quaternary  
684 sedimentary succession. ~~These two units are separated by a weak mechanical layer~~  
685 ~~composed of Triassic evaporites. These lithologies–Triassic evaporites~~ are well  
686 documented for their ductile ~~behaviour~~behaviour, which enables them to act as  
687 regional detachment layers (e.g., Morley et al., 2003; Jackson and Hudec, 2005) and  
688 inhibits the propagation of faults (e.g., Withjack et al., 1990; Pascoe et al., 1999;  
689 Maurin and Niviere, 2000; Withjack and Callaway, 2000; Richardson et al., 2005;  
690 Ford et al., 2007; Kane et al., 2010; Marsh et al., 2010). Moreover, mechanically weak  
691 layers have been shown to induce full or partial geometric and kinematic decoupling  
692 between sub- and supradetachment successions (e.g., Stewart et al., 1997;  
693 Withjack and Callaway, 2000; Ford et al., 2007; Tvedt et al. 2013). In this section, we  
694 focus on the implications of this mechanical arrangement in terms of ~~the-how the~~  
695 ~~presence of a weak mechanical layer influence the vertical propagation of seismic~~  
696 ~~rupturesseismic potential of salt-influenced active faults.~~

697 In an active region, tectonics are generally the main driving mechanism of fault  
698 displacement. However, in the case of salt-influenced faults, displacement can  
699 also result from salt withdrawal. Our analysis of the evolution of the Cullera Fault  
700 presented in the previous section indicates that the fault offset is related to the  
701 interplay between two mechanisms: tectonic offset along the fault and  
702 displacement related to salt withdrawal. Our analysis also reveals how these two  
703 processes interact with each other. Consequently, in areas with salt-influenced  
704 faults, seismicity can potentially be produced from either mechanism or a  
705 combination of both.

706 In terms of seismic potential, there is a significant difference between a tectonic  
707 earthquake and a salt-withdrawal earthquake. This difference lies in the maximum  
708 potential thickness of the seismogenic layer involved in the rupture. ~~Tectonic stress~~  
709 ~~affects the entire crust; therefore, strain related to tectonic accumulates both in the~~

710 suprasalt and subsalt successions. Consequently, a tectonically driven  
711 earthquake could theoretically rupture the entire seismogenic crust. In contrast, a  
712 salt withdrawal-related earthquake would imply offset restricted to the suprasalt  
713 succession, as in this case displacement surface coalesces into the salt layer.  
714 Therefore, in an earthquake restricted to the suprasalt succession, the thickness of  
715 the seismogenic layer is limited by the depth of the mechanically weak layer,  
716 reducing the maximum potential rupture area and, consequently, the seismic  
717 potential. A salt-withdrawal-related earthquake could induce a vertical stress drop  
718 related to salt displacement, potentially triggering displacement in the subsalt  
719 succession and leading to a complex rupture. ~~However, in terms of seismic~~  
720 ~~potential, such a hypothetical earthquake would not differ from a tectonically-~~  
721 ~~driven event.~~ Similarly, a tectonically driven earthquake may rupture only the  
722 suprasalt succession.

723 Despite the mechanism driving seismicity, the presence of a weak mechanical layer  
724 within the seismogenic crust significantly influences the seismogenic potential of  
725 active faults. We hypothesise that this weak layer could locally hinder the effective  
726 vertical propagation of a rupture, thereby resulting in faults being seismogenically  
727 bounded. Specifically, the total or partial decoupling induced by the weak evaporitic  
728 layer may limit the effective width of the seismogenic layer. This hypothesis is  
729 independent of the weak layer composition; therefore, our hypothesis can be  
730 extended to any region with a similar structural configuration.

731 Significant earthquakes ( $M_w > 6$ ) typically nucleate at depths greater than 5 km.  
732 However, recent events in central Italy and France have demonstrated that very  
733 shallow (2–5 km) earthquakes of moderate magnitude ( $M_w$  5–6) can also occur  
734 (Chiaraluce et al., 2017; Godano et al., 2025; Improta et al., 2019). In the  
735 southwestern Valencia Trough, the thickness of the supra-salt succession is slightly  
736 less than 5 km. Therefore, while the probability of a significant earthquake  
737 nucleating within the supra-salt succession is low, it is not zero. In this section we  
738 evaluate the seismic potential of these (unlikely) supra-salt ruptures.

739 The case of central Italy could be taken as a geologic and tectonic analogues of the  
740 southwestern Valencia Trough. Central Italy resembles the southwestern Valencia

**Con formato:** Fuente: (Predeterminada) +Cuerpo (Aptos), 12 pto, Color de fuente: Texto 1, Ligaduras: Estándar + Contextual

**Con formato:** Inglés (Estados Unidos)

**Con formato:** Fuente: (Predeterminada) +Cuerpo (Aptos), 12 pto, Color de fuente: Texto 1, Ligaduras: Estándar + Contextual

**Con formato:** Fuente: (Predeterminada) +Cuerpo (Aptos), 12 pto, Color de fuente: Texto 1, Ligaduras: Estándar + Contextual

741 Trough as both regions are presently dominated by extensional tectonics, and both  
742 are characterised by a pronounced mechanical layering in the upper crust.  
743 Recently, central Italy has undergone high seismicity, including the 1997-1998  
744 Umbria-Marche, 2009 L'Aquila, and 2016-2017 Amatrice-Norcia seismic sequences  
745 (Chiaraluze et al., 2003; Valoroso et al., 2013 Chiaraluze et al., 2017; Improta et al.,  
746 2019; Michele et al., 2020). The area of central Italy where these seismic sequences  
747 took place is characterized by a complex geological framework consisting of several  
748 geological domains. Most of this area belongs to the Umbria-Marche fold-and-  
749 thrust belt. This belt consists of a crystalline basement overlain by a 3-8-km-thick  
750 Mesozoic-Quaternary sedimentary cover (Menichetti and Coccioni, 2013). The  
751 sedimentary Mesozoic succession starts with a 1.2 km thick salt layer (Anidriti di  
752 Burano Formation; Martinis and Pieri, 1964) acting as a mechanical weak layer. That  
753 is, similar to the southwestern Valencia Trough, the seismogenic crust of central  
754 Italy is characterised by the presence of a mechanically weak layer. As a  
755 consequence of thrusting during the Miocene-Pliocene, this weak layer is vertically  
756 repeated in some sectors (Barchi et al., 2021). Therefore, in central Italy the  
757 seismogenic crust includes from one to three weak layers.

758 Central Italy undergoes extension responsible for normal active faults. These active  
759 normal faults are the seismogenic sources of the seismic sequences occurred in  
760 the last decades (e.g., Boncio et al., 2004; Barchi and Mirabella, 2009), as well as  
761 several historical events (Rovida et al., 2020). Normal active faults in central Italy  
762 present a listric geometry in the sedimentary cover and offset the top of the  
763 basement (Barchi et al., 2021). The 1997-1998 Umbria- Marche and 2016-2017  
764 Amatrice-Norcia seismic sequences nucleated within the suprasalt succession,  
765 including main events (Mw 5-6) with very shallow centroids (3-4 km; Barchi et al.,  
766 2021).

767 Based on the tectonic and stratigraphic similarities above exposed, we propose that  
768 the southwestern Valencia Trough may exhibit a comparable pattern of seismicity to  
769 that of central Italy. Specifically, we hypothesise that seismic events in the  
770 southwestern Valencia Trough could also have nucleated within the suprasalt  
771 succession and in the basement. Furthermore, we postulate that large earthquakes

Con formato: Fuente: 12 pto

Con formato: Fuente: 12 pto

772 in the southwestern Valencia Trough could also rupture both mechanical layers.  
773 Available centroid data for the southwestern Valencia Trough suggest that most  
774 earthquakes nucleate at depths between 1 and 13 km (Fig. 2). Although these depth  
775 estimates carry significant uncertainties, we interpret this dataset as supporting  
776 evidence for our hypothesis that seismicity in the southwestern Valencia Trough  
777 nucleates both in the basement and in the cover.

778 From this hypothesis we evaluate the seismic potential of these (unlikely) supra-salt  
779 ruptures. A widely used approach to characterise the seismic potential of an active  
780 fault involves earthquake fault scaling relationships. These relationships estimate  
781 the seismic parameters of an active fault ~~on the basis of~~ based on its geometric  
782 and/or kinematic features (Kanamori and Anderson, 1975; Geller, 1976; Wells and  
783 Coppersmith; 1994; Stirling et al., 2002 and 2013; Leonard, 2010 and 2014; among  
784 many others). In the case of the southwestern Valencia Trough faults, the available  
785 data support characterisation on the basis of geometric features, such as fault area,  
786 length, or width. However, the mechanical layering observed in the southwestern  
787 Valencia Trough necessitates the cautious application of these scaling  
788 relationships. The influence of the weak mechanical layer introduces complexities  
789 that may not be fully accounted for by traditional scaling methods.

790 ~~Therefore, we begin our analysis by comparing the southwestern Valencia Trough~~  
791 ~~with the Zagros fold-and-thrust belt. While Zagros fold-and-thrust belt differs~~  
792 ~~tectonically from the southwestern Valencia Trough, as it is dominated by~~  
793 ~~shortening rather than extension, it structurally resembles the southwestern~~  
794 ~~Valencia Trough because of its pronounced mechanical layering in the upper crust.~~  
795 ~~The Zagros fold-and-thrust belt features a crystalline basement overlain by a 10-km-~~  
796 ~~thick Precambrian-Quaternary sedimentary cover. These two successions are~~  
797 ~~separated by the Hormuz salt layer (Casciello et al., 2009; Sherkaty et al., 2005;~~  
798 ~~Molinaro et al., 2005). That is, similar to the southwestern Valencia Trough, the~~  
799 ~~seismogenic crust is characterised by the presence of an intermediate~~  
800 ~~mechanically weak layer. Seismicity in the Zagros fold-and-thrust belt is~~  
801 ~~characterised by a general absence of coseismic surface ruptures. This seismicity~~  
802 ~~nucleates both in the basement and in the cover (Nissen et al., 2011). Notably, the~~

803 centroids of most of the larger events (magnitudes exceeding  $M_w$  5), are located at  
804 depths between 4 and 14 km, indicating that seismic activity nucleates both within  
805 the suprasalt succession and in the basement (Nissen et al. 2007, 2010; Roustaei  
806 et al. 2010). Additionally, very large earthquakes have occurred in the Zagros fold-  
807 and-thrust belt; these earthquakes include the Ghir and Khurgu events ( $M_w$  6.7);  
808 which are interpreted as ruptures involving both the basement and the cover,  
809 rupturing through the basement-cover interface (Nissen et al., 2011).

810 We propose that the southwestern Valencia Trough may exhibit a comparable  
811 pattern of seismicity to that of the Zagros fold-and-thrust belt. Specifically, we  
812 hypothesise that seismic events in the southwestern Valencia Trough could have  
813 nucleated within both the basement and the suprasalt succession. Furthermore, we  
814 postulate that larger earthquakes in the southwestern Valencia Trough could also  
815 rupture both mechanical layers. Available centroid data for the southwestern  
816 Valencia Trough suggest that most earthquakes nucleate at depths between 1 and  
817 13 km (Fig. 2). Although these depth estimates carry significant uncertainties, we  
818 interpret this dataset as supporting evidence for our hypothesis that seismicity in  
819 the southwestern Valencia Trough nucleates both in the basement and in the cover.

820 As we mentioned previously, most empirical source-scaling relationships for crustal  
821 earthquakes correlate the moment magnitude ( $M_w$ ) with the fault dimensions  
822 (length, width, and/or area; (Kanamori and Anderson, 1975; Geller, 1976; Wells and  
823 Coppersmith; 1994; Stirling et al., 2022; Leonard, 2010; among many others). We  
824 propose that when these scaling relationships are applied to regions with a weak  
825 mechanical layer, the role of this layer should be explicitly considered in the  
826 analysis. This is because the presence of a weak layer can potentially hinder the  
827 effective vertical propagation of a rupture, thereby limiting the effective width of the  
828 seismogenic layer. This consideration is particularly relevant for earthquakes that  
829 nucleate above the weak layer. We propose including a correction factor in the  
830 empirical relationships that explicitly accounts for cases where earthquakes are  
831 more likely to involve only part of the seismogenic layer due to mechanical  
832 heterogeneities within the crust. This factor would aim to provide a more accurate  
833 seismic characterization of faults in regions with such a structural arrangement.

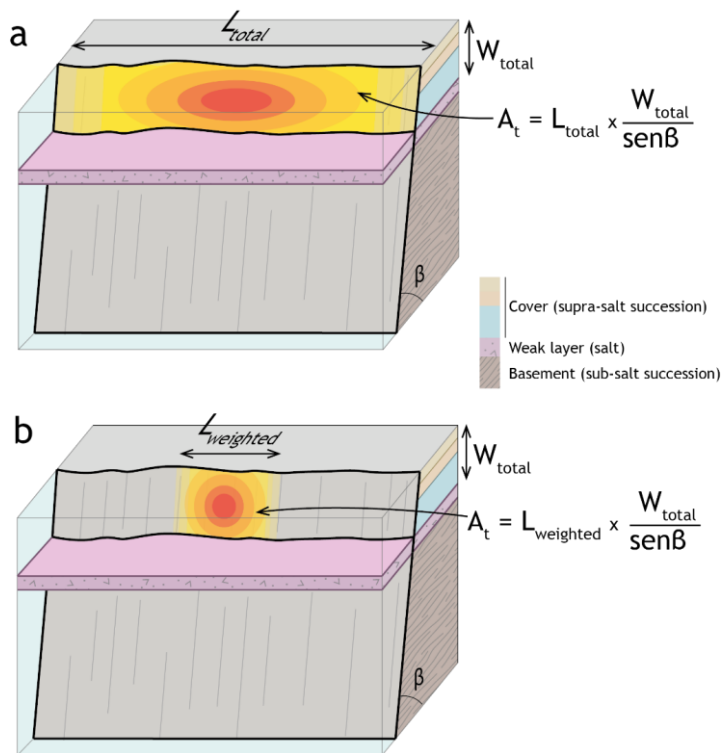
834

835 Several studies suggest that the downdip width of the seismogenic crust (the  
836 thickness of seismogenic crust measured along the fault plane) can constrain the  
837 maximum magnitudes of earthquakes (Hyndman, 2007; Ruff and Kanamori, 1983;  
838 Weng & Yang, 2017). For large-magnitude events involving the entire seismogenic  
839 crust, some scaling relationships account for the constraint on fault-width rupture  
840 growth relative to fault-length rupture growth by incorporating a change in slope in  
841 width-to-length scaling (Leonard, 2010; Yen and Ma, 2011; Leonard, 2014; Cheng et  
842 al., 2019; Huang et al., 2024). This change in slope reflects the width of the  
843 seismogenic crust, which imposes a limit on rupture propagation owing to  
844 variations in the mechanical behaviour of the crust. We propose a similar approach  
845 to evaluate the seismic potential of regions characterised by a weak mechanical  
846 layer within the upper crust, such as the southwestern Valencia Trough.

847 Our approach involves including the rupture aspect ratio when calculating the  
848 geometric parameters of an active fault. Specifically, we propose that, instead of  
849 using the total area or length of the fault as direct inputs to scaling relationships, a  
850 correction factor should be applied to these geometric parameters. This correction  
851 factor is based on the empirical aspect ratio of faults. For example, consider an  
852 earthquake nucleating above a weak mechanical layer. Two potential scenarios for  
853 the propagation of such an earthquake can be envisioned: i) that it propagates  
854 through the basement–cover interface or ii) that it remains restricted to the  
855 succession above the weak layer. In the first scenario, the potential maximum  
856 rupture area can be calculated by multiplying the fault length by the fault width. Any  
857 area-based or length-based scaling relationship can then be applied. This scenario  
858 represents the maximum seismic potential of the fault.

859 In the second scenario, where rupture propagation is restricted to succession above  
860 the weak layer, a simplistic calculation of the fault area would multiply the total fault  
861 length by the thickness of the ruptured succession (Fig 11). However, since the  
862 hypothesised rupture offsets only the succession above the mechanically weak  
863 layer, the width of the rupture is significantly limited. This would result in a highly  
864 elongated rupture with an unusually high aspect ratio, deviating from commonly

865 observed values (Nicol et al., 1996; Stock & Smith, 2000). For this second scenario,  
 866 we propose using the thickness of the ruptured succession as a limiting factor.  
 867 Specifically, the rupture area should be calculated by multiplying the width of the  
 868 fault **offset** (based on the thickness of the succession above the weak layer and  
 869 corrected by the fault dip) by the total fault length weighted by the aspect ratio (Fig  
 870 11). This weighted area can then be used as input in any area-based scaling  
 871 relationship. We consider that this calculation offers a more realistic estimation of  
 872 the maximum seismogenic potential for events rupturing only the succession above  
 873 the weak layer. Finally, we recommend avoiding length-based scaling relations for  
 874 this second scenario, as such relations implicitly assume a rupture of the entire  
 875 seismogenic crust.



876  
 877 Figure 11. Conceptual model of the weighted rupture area of an earthquake  
 878 nucleating above the weak mechanical layer. The area of the rupture is  
 879 shown using a red–yellow gradient. An earthquake rupturing the total fault

880 length ( $L$ ) and the total thickness ( $W_{\text{total}}$ ) above the weak layer would result in  
881 nonrealistic, highly elongated ruptures. In figure panel b, we propose a more  
882 realistic case: an earthquake offsetting the total thickness above the weak  
883 layer ( $W_{\text{total}}$ ) and a rupture length weighted by the aspect ratio ( $L_w$ ).

884

885

886 **8. Seismic characterisation of active faults in the southwestern Valencia**  
887 **Trough.**

888 In this section, we compute the seismic potential of the active faults in the  
889 southwestern Valencia Trough by applying several scaling relationships. We perform  
890 two distinct calculations corresponding to the two scenarios described earlier. i) In  
891 the first scenario, we assume a rupture involving both the supra- and subsalt  
892 successions. That is, this first scenario accounts for an earthquake rupturing the  
893 entire seismogenic crust. This scenario provides the maximum seismic potential of  
894 the faults. ii) In the second scenario, we assume that a rupture is restricted to the  
895 suprasalt succession. For this calculation, we apply several area-based scaling  
896 relationships, and we use the area weighted by the aspect ratio as the input  
897 parameter. Since the rupture area involved in this second scenario is relatively  
898 small, a relatively low seismogenic potential is expected.

899

900 *8.1. First scenario: Ruptures involving the entire seismogenic crust.*

901 For both scenarios, we apply the scaling relationships of Wells & Coppersmith  
902 (1994) (values corresponding to normal faults [for the Cullera and Valencia faults,](#)  
903 [and to strike slip faults for the Albufera Fault](#)) and Stirling et al. (2002). In the first  
904 scenario, i.e., ruptures involving the entire seismogenic crust, we assume that a  
905 complete fault ruptured from the subsalt basement through the suprasalt  
906 succession. [To compute the seismogenic potential of this first scenario we used the](#)  
907 [fault length and fault area as the primary input parameter \(Table 1\). The fault area](#)  
908 [used for these calculations was the result of multiplying the fault length by the fault](#)  
909 [width. We prefer to use this simplification instead of the areas calculated from our](#)  
910 [3D models to ensure consistency when comparing magnitude estimates derived](#)  
911 [from the methodology involving a correction factor \(see below\). Since the total](#)  
912 [thickness of the seismogenic crust in the study area is not precisely known,](#)  
913 [García-Mayordomo, \(2005\) proposed a thickness ranging between 9 and 11 km.](#)  
914 [This value agrees with crust thicknesses based on deep seismic profiles \(Etheve et](#)  
915 [al., 2016; Maillard & Mauffret, 2013; Ramos et al., 2025\) as well as the lithospheric](#)

Con formato: Inglés (Estados Unidos)

916 structure based on P-wave receiver function analysis and seismic tomography  
 917 (Mancilla et al., 2015; Palomeras et al., 2017). we used the fault length as the primary  
 918 input parameter for these calculations (Table 1). Therefore, we assumed a mean  
 919 thickness of the seismogenic crust of 10 km.

920

921

922 Table 1 Source parameters obtained from length- and area-based scaling  
 923 relationships (Wells & Coppersmith, 1994 -WC94- and Stirling et al., 2002 -  
 924 Stirling02-) assuming ruptures involving the entire seismogenic crust. L, fault length;  
 925 M<sub>w</sub>, moment magnitude; AD, average displacement; MD, maximum displacement.  
 926 Values computed using length-based Wells & Coppersmith (1994) relationships  
 927 refer to normal faulting (Cullera and Valencia faults) and strike-slip faulting (Albufera  
 928 Fault).

Con formato: Subíndice

	Length-based relationships						Area-based relationships		
	L km	WC94			Stirling02		A km <sup>2</sup>	WC94	Stirling02
		M <sub>w</sub>	AD-m	MD-m	M <sub>w</sub>	AD-m		M <sub>w</sub>	M <sub>w</sub>
Cullera Fault	59	7.2 ±0.34	1.61 ±0.37	4.94 ±0.41	7.3 ±0.30	2.39 ±0.24	834.4	6.91 ±0.25	7.22 ±0.26
Albufera Fault	40	6.97 ±0.34	0.99 ±0.37	2.75 ±0.41	7.16 ±0.30	2.23 ±0.24	565.7	6.74 ±0.25	7.1 ±0.26
Valencia Fault	20	6.58 ±0.34	0.42 ±0.37	0.97 ±0.41	6.92 ±0.30	1.97 ±0.24	282.9	6.43 ±0.25	6.88 ±0.26

929

Input parameters	WC94			Stirling02		
	L-km	M <sub>w</sub>	AD-m	MD-m	M <sub>w</sub>	AD-m

Con formato: Justificado

Tabla con formato

Cullera Fault	59	7.2 ±0.34	1.61 ±0.37	4.94 ±0.41	7.3 ±0.30	2.39 ±0.24
Albufera Fault	20	6.58 ±0.34	0.42 ±0.37	0.97 ±0.41	6.92 ±0.30	1.97 ±0.24
Valencia Fault	40	6.97 ±0.34	0.99 ±0.37	2.75 ±0.41	7.16 ±0.30	2.23 ±0.24

Con formato: Justificado

Con formato: Justificado

Con formato: Justificado

930

## 931 8.2. Second scenario: Ruptures involving only the suprasalt succession

932 In this scenario, the presence of a mechanically weak layer within the seismogenic  
933 crust is considered to control the seismic potential of active faults. As discussed  
934 previously, we use the weighted rupture area as the input parameter for the scaling  
935 relationships. The weighting factor is based on the aspect ratio of normal faults. To  
936 provide context for this approach, we also present seismic parameters calculated  
937 from the total fault area offsetting the entire suprasalt succession. The aspect ratios  
938 of normal fault ruptures vary widely (0.4–18); however, most of the observed  
939 ruptures are within the range of 0.5 to 3.5 (Nicol et al., 1996; Stock & Smith, 2000),  
940 with a mode value of 1.8 (30%, Stock & Smith, 2000). Numerical simulations of  
941 strike-slip faults by Weng & Yang (2016) demonstrated that the width of the  
942 seismogenic layer significantly influences the rupture aspect ratios. According to  
943 their findings, a seismogenic layer thickness of approximately 10 km marks a critical  
944 boundary: for thicknesses less than this value, rupture aspect ratios remain low (ca.  
945 2), whereas thicknesses greater than 10 km result in significantly higher aspect  
946 ratios (<8). Considering these findings and given that the suprasalt succession in the  
947 southwestern Valencia Trough has an average thickness of approximately 5 km, we  
948 adopt an aspect ratio of 1.8 for our calculations.

949 In the southwestern Valencia Trough, the suprasalt succession thickness at the  
950 location of active faults varies. We used thicknesses of 5 km, 3.3 km and 2.3 km for  
951 the Cullera, Valencia, and Albufera faults respectively, as input values for our  
952 calculation. (~5 km) and an average fault dip of ~45° yield a maximum rupture width

953 of approximately 7.1 km for events confined to the suprasalt succession. For events  
 954 unrestricted by the aspect ratio (i.e., earthquakes rupturing the entire fault length  
 955 and width of the suprasalt succession), we compute the rupture area as the product  
 956 of length and width accounting also for the fault dip ( $L*W/\sin\beta$ ). However, when the  
 957 seismic potential for ruptures weighted by the aspect ratio is calculated, the  
 958 controlling factor is the fault width. As we assume a constant thickness for the  
 959 suprasalt succession across southwestern Valencia Trough, the rupture area and  
 960 corresponding seismic potential are consistent for all the faults in this study (Table  
 961 2):

962  
 963 Table 2 Moment magnitude obtained from scaling relationships (Wells &  
 964 Coppersmith, 1994 -WC94- and Stirling et al., 2002 -Stirling02-). The first column  
 965 (not weighted area) corresponds to the values obtained assuming ruptures involving  
 966 the total suprasalt succession. The second column (weighted area) shows the  
 967 values obtained using the area weighted by the aspect ratio as input parameter.

968

	Not-weighted area			Weighted area		
	input parameters	M <sub>w</sub>	M <sub>w</sub>	input parameters	M <sub>w</sub>	M <sub>w</sub>
	A km <sup>2</sup>	WC94	Stirling02	A km <sup>2</sup>	WC94	Stirling02
Gulltera Fault	511.4	6.69 ±0.34	7.07 ±0.26	135.2	6.10 ±0.34	6.65 ±0.26
Atbufera Fault	346.7	6.56 ±0.34	6.72 ±0.26	135.2	6.10 ±0.34	6.65 ±0.26
Valencia Fault	173.4	6.21 ±0.34	6.94 ±0.26	135.2	6.10 ±0.34	6.65 ±0.26

969

970

971

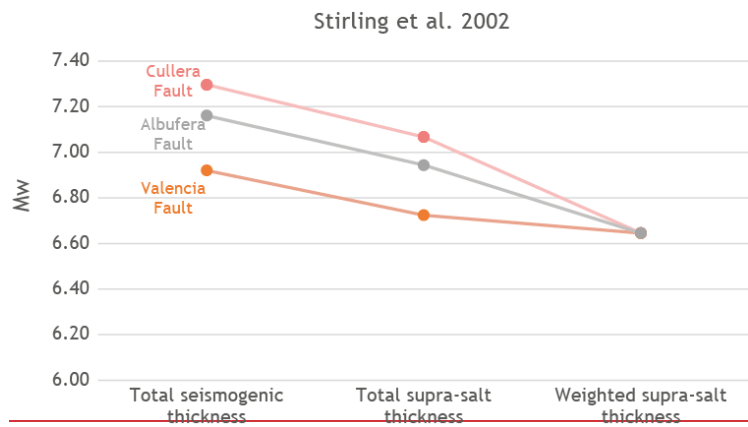
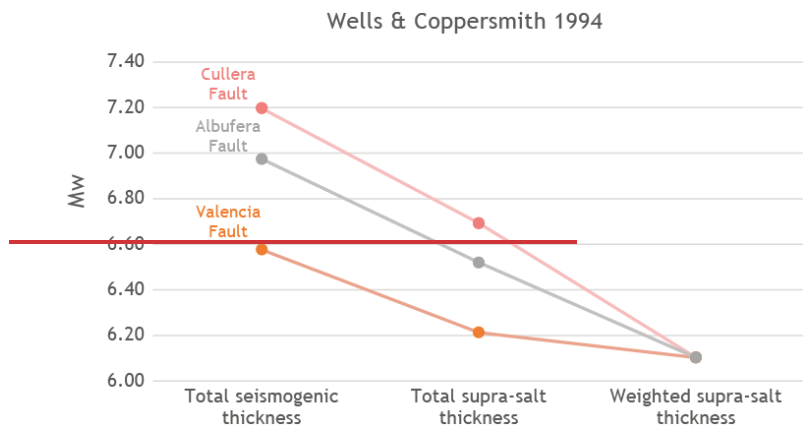
972

	Not weighted area			Weighted area		
	Input parameters	$M_w$	$M_w$	Input parameters	$M_w$	$M_w$
	A km <sup>2</sup>	WC94	Stirling02	A km <sup>2</sup>	WC94	Stirling02
Cullera Fault	360	6.54 ± 0.34	6.96 ± 0.26	67	5.79 ± 0.34	6.42 ± 0.26
Albufera Fault	112	6.02 ± 0.34	6.59 ± 0.26	14	5.16 ± 0.34	5.93 ± 0.26
Valencia Fault	81	5.87 ± 0.34	6.48 ± 0.26	29	5.42 ± 0.34	6.16 ± 0.26

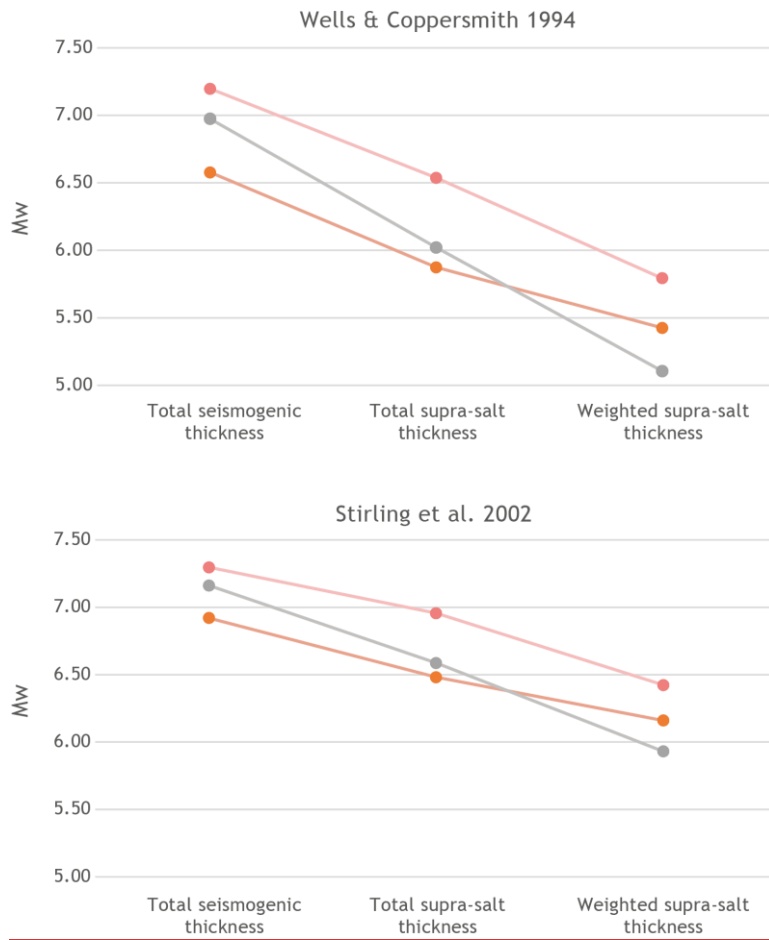
973

974 The comparison between the standard application of earthquake source scaling  
975 relations and the approach presented here for regions characterised by the  
976 presence of a weak mechanical layer within the seismogenic crust reveals  
977 significant differences (Fig. 12). The maximum expected magnitudes for  
978 characteristic events rupturing the entire seismogenic crust (i.e., propagating  
979 across the basement–cover interface) are estimated to be ~~7.26~~~~9~~–7.3, ~~6.584~~–6.92,  
980 and ~~6.977~~–~~7.16~~–2 for the Cullera, Valencia, and Albufera Faults, respectively. In  
981 contrast, for hypothetical earthquakes restricted to the suprasalt succession and  
982 rupturing of the total length of the faults, the expected magnitudes are lower, ranging  
983 from ~~6.54~~–6.96, ~~5.87~~–6.48, ~~6.02~~–6.59 ~~6.7~~–7.1, ~~6.2~~–6.7, and ~~6.5~~–6.9 for the Cullera,  
984 Valencia, and Albufera faults, respectively. However, in such cases, we argue that  
985 the seismic potential derived using area-weighted relations provides a more  
986 realistic estimate. Using this approach, our calculations yield maximum  
987 magnitudes of ~~5.79~~–6.42, ~~5.42~~–6.16, and ~~5.11~~–5.93 for the Cullera, Valencia, and  
988 Albufera faults, respectively ~~6.1~~–6.7 for all faults. These values are ~~2~~–95–15 % lower  
989 than those obtained when accounting for the total suprasalt succession thickness.

990 When the area-weighted values are compared with the maximum expected  
 991 magnitudes for ruptures involving the entire seismogenic crust, the results reveal a  
 992 ~~4-15~~11-26% reduction. This discrepancy highlights the importance of incorporating  
 993 mechanical layering into seismic potential assessments in regions where weak  
 994 layers influence fault dynamics and rupture propagation. Furthermore, these  
 995 differences in seismic potential should be addressed in probabilistic seismic hazard  
 996 assessments.



997



998

999 Figure 12. Plots of  $M_w$  values for the Cullera, Albufera and Valencia Faults obtained  
 1000 using the scaling relationships of Wells & Coppersmith (1994) and Stirling et al.  
 1001 (2002). The plots show the values computed assuming a rupture of the total  
 1002 seismogenic thickness, a rupture of the total suprasalt succession, and the values  
 1003 assuming a rupture of an area calculated using a suprasalt thickness weighted with  
 1004 the aspect ratio.

1005

## 1006 **9. Conclusions:**

1007 Analysis of a comprehensive subsurface dataset from the southwestern Valencia  
1008 Trough enables the identification of three major active ~~normal~~-faults: the ~~normal~~  
1009 Cullera ~~Fault~~, ~~the oblique~~ Albufera ~~Fault~~, and ~~the normal~~ Valencia ~~faults~~~~Fault~~.  
1010 Among these faults, the Cullera Fault is the main active structure in this region, with  
1011 a cumulative offset of 1800 m at the top of the Messinian marker. The long-term slip  
1012 rate varies over time between  $0.15 \pm 0.1$  mm/y and  $0.4 \pm 0.1$  mm/y. The Albufera Fault,  
1013 which is 55 km in length, has a long-term slip rate of  $0.2 \pm 0.1$  mm/y, whereas the 20-  
1014 km-long Valencia Fault significantly influences the spatial distribution of  
1015 Quaternary depocentres.

1016 Our results also reveal ~~a 10-km-thick~~ heterogeneous seismogenic crust in the study  
1017 area, largely because of a mechanically weak layer, which is composed mainly of  
1018 Triassic evaporites. Consequently, two competing mechanisms are responsible for  
1019 the offset along the active faults: tectonics and salt withdrawal. A quantitative  
1020 evolutionary analysis of the Cullera Fault indicates that tectonics was the dominant  
1021 mechanism during the Pliocene, whereas salt withdrawal took precedence in the  
1022 early Quaternary (2.6–2 Ma). After 2 Ma, tectonic activity once again became the  
1023 primary driver of fault displacement.

1024 ~~Using standard scaling relationships, we computed maximum expected~~  
1025 ~~magnitudes for the southwestern Valencia Trough faults. These maximum expected~~  
1026 ~~magnitudes range between 6.9-7.3 for the Cullera Fault, 6.7-7.2 for the Albufera~~  
1027 ~~Fault, and 6.4-6.9 for de Valencia Fault. However, the~~~~The~~ mechanically layered crust  
1028 of the southwestern Valencia Trough influences seismicity: events may nucleate in  
1029 either the basement or the suprasalt succession. ~~Moreover, the weak layer could~~  
1030 ~~influence the vertical propagation of a potential rupture. That is, ~~Total~~total or partial~~  
1031 decoupling related to the mechanically weak layer implies that an earthquake that  
1032 nucleated in the suprasalt succession would likely be restricted to this upper part of  
1033 the seismogenic crust, yet larger events involving basement and cover units are also  
1034 plausible. For reliable seismic hazard assessments, both scenarios must be  
1035 accounted for. To compute the seismogenic potential of active faults under the  
1036 assumption of rupture within the suprasalt succession, we propose the use of the

1037 rupture aspect ratio as a correction factor for the maximum rupture area.  
1038 Specifically, the product of the suprasalt thickness (corrected by the fault dip) and  
1039 the fault length—weighted by the aspect ratio—provides a more realistic  
1040 approximation of the maximum rupture area. Using this method, the maximum  
1041 magnitudes for suprasalt ruptures of the southwestern Valencia Trough faults are  
1042 5.79-6.42, 5.42-6.16, and 5.11-5.93 for the Cullera, Valencia, and Albufera faults,  
1043 respectively. These values are ~~2-95-15~~% lower than those obtained by considering  
1044 the full suprasalt thickness alone, and ~~4-1511-26~~% lower than estimates involving  
1045 the entire seismogenic crust.

1046 Overall, these findings greatly enhance our understanding of the seismogenic  
1047 potential of the southwestern Valencia Trough, an offshore area near densely  
1048 populated areas. These findings provide a basis for improved seismic hazard  
1049 assessments. Additionally, as we are addressing offshore faults exhibiting vertical  
1050 displacement, our findings can be used to establish the tsunamigenic potential of  
1051 this region. Furthermore, this approach for incorporating mechanical  
1052 heterogeneities in the seismogenic crust can be applied to other regions and  
1053 tectonic settings with analogous structural configurations.

1054

1055

1056 **10. Author contribution**

1057 Martin-Rojas, I.: Conceptualization, Data curation, Formal analysis, Funding  
1058 acquisition, Investigation, Methodology, Project administration, Supervision,  
1059 Validation, Visualization, Writing – original draft preparation, review & editing

1060 Ramos, A.: Data curation, Formal analysis, Funding acquisition, Investigation,  
1061 Resources, Visualization, Writing – original draft preparation, review & editing

1062 De Ruig, M.: Data curation, Formal analysis, Investigation, Resources,  
1063 Visualization, Writing – original draft preparation, review & editing

1064 Medina-Cascales, I.: Data curation, Formal analysis, Investigation, Visualization,  
1065 Writing – review & editing

1066 Santamaría-Pérez, E.: Data curation, Formal analysis, Investigation, Writing –  
1067 review & editing

1068 Alfaro, P.: Data curation, Formal analysis, Investigation, Supervision, Writing –  
1069 review & editing

1070

1071 **11. Competing interests**

1072 The authors declare that they have no conflict of interest.

1073

1074 **12. Acknowledgements**

1075 We acknowledge the comments of the Raúl Pérez-López, an anonymous ~~XXXX~~  
1076 reviewer, ~~s~~ and the Editor Solmaz Mohadjer ~~XXXX~~, which significantly improved the  
1077 quality of this paper.

Con formato: Sin Resaltar

Con formato: Inglés (Estados Unidos)

Código de campo cambiado

1078

1079 **13. Financial support**

1080 This research was funded by the Spanish Ministry of Science, Innovation and  
1081 University (research projects PID2021-127967NB-I00 and RTI2018-100737-B-I00),  
1082 Generalitat Valenciana (Valencian Regional Government, research projects  
1083 AICO2021/196 and CIAPOS/2022/082, and University of Alicante (research project  
1084 VIGROB053). The authors acknowledge the use of the MOVE Software Suite granted  
1085 by PE Limited (Petex).



1087

References

1088 Agustí, J., Santos-Cubedo, A., Furió, M., De Marfá, R., Blain, H., Oms, O., & Sevilla, P.

1089 (2011). The late Neogene-early Quaternary small vertebrate succession from the

1090 Almenara-Casablanca karst complex (Castellón, Eastern Spain): Chronologic and

1091 paleoclimatic context. *Quaternary International*, 243(1), 183–191.

1092 10.1016/j.quaint.2010.11.016

1093 Albarracín, S., Alcántara-Carrió, J., Barranco, A., Sánchez García, M. J., Fontán Bouzas, Á,

1094 & Rey Salgado, J. (2013). Seismic evidence for the preservation of several stacked

1095 Pleistocene coastal barrier/lagoon systems on the Gulf of Valencia continental shelf

1096 (western Mediterranean). *Geo-Marine Letters*, 33(2-3), 217–223. 10.1007/s00367-

1097 012-0315-x

1098 Arche, A., & López-Gómez, J. (1996). Origin of the Permian-Triassic Iberian Basin, central-

1099 eastern Spain. *Tectonophysics*, 266(1), 443–464. 10.1016/S0040-1951(96)00202-8

Con formato: Italiano (Italia)

1100 [Barchi, M. R., Carboni, F., Michele, M., Ercoli, M., Giorgetti, C., Porreca, M., Azzaro, S., &](#)

1101 [Chiaraluca, L. \(2021\). The influence of subsurface geology on the distribution of](#)

Con formato: Inglés (Estados Unidos)

1102 [earthquakes during the 2016–2017 Central Italy seismic sequence. \*Tectonophysics\*,](#)

1103 [807, 228797. https://doi.org/10.1016/j.tecto.2021.228797](#)

1104 [Barchi, M. R., & Mirabella, F. \(2009\). The 1997–98 Umbria–Marche earthquake sequence:](#)

Con formato: Inglés (Estados Unidos)

1105 [“Geological” vs. “seismological” faults. \*Tectonophysics\*, 476\(1–2\), 170–179.](#)

Con formato: Inglés (Estados Unidos)

1106 [https://doi.org/10.1016/j.tecto.2008.09.013](#)

Con formato: Inglés (Estados Unidos)

Con formato: Inglés (Estados Unidos)

1107 [Boncio, P., Lavecchia, G., & Pace, B. \(2004\). Defining a model of 3D seismogenic sources](#)

Código de campo cambiado

1108 [for Seismic Hazard Assessment applications: The case of central Apennines \(Italy\).](#)

- 1109 [Journal of Seismology, 8\(3\), 407–425.](#)
- 1110 <https://doi.org/10.1023/B:JOSE.0000038449.78801.05>
- 1111 Bufor, E., & Udías, A. (2021). *El terremoto de Alcoy de 1620 y la serie sísmica de 1644 en*
- 1112 *la comarca de Muro*. Centro Nacional de Información Geográfica.
- 1113 Bufor, E., Udías, A., Sanz de Galdeano, C., & Cesca, S. (2015). The 1748 Montesa
- 1114 (southeast Spain) earthquake — A singular event. *Tectonophysics*, 664, 139–153.
- 1115 10.1016/j.tecto.2015.09.005
- 1116 Cameselle, A. L., Urgeles, R., De Mol, B., Camerlenghi, A., & Canning, J. C. (2014). Late
- 1117 Miocene sedimentary architecture of the Ebro Continental Margin (Western
- 1118 Mediterranean): implications to the Messinian Salinity Crisis. *International Journal of*
- 1119 *Earth Sciences : Geologische Rundschau*, 103(2), 423–440. 10.1007/s00531-013-
- 1120 0966-5
- 1121 Casciello, E., Vergés, J., Saura, E., Casini, G., Fernández, N., Blanc, E., Homke, S., & Hunt,
- 1122 D. W. (2009). Fold patterns and multilayer rheology of the Lurestan Province, Zagros
- 1123 simply folded belt (Iran). *Journal of the Geological Society*, 166(5), 947–959.
- 1124 10.1144/0016-76492008-138
- 1125 Cheng Jia, C. J., Rong, Y., Magistrale, H., Chen Guihua, C. G., & Xu Xiwei, X. X. (2019a).
- 1126 Earthquake rupture scaling relations for mainland China. *Seismological Research*
- 1127 *Letters*, 91(1), 248–261. 10.1785/0220190129
- 1128 Cheng Jia, C. J., Rong, Y., Magistrale, H., Chen Guihua, C. G., & Xu Xiwei, X. X. (2019b).
- 1129 Earthquake rupture scaling relations for mainland China. *Seismological Research*
- 1130 *Letters*, 91(1), 248–261. 10.1785/0220190129

Con formato: Italiano (Italia)

- 1131 [Chiaraluca, L., Di Stefano, R., Tinti, E., Scognamiglio, L., Michele, M., Casarotti, E.,](#)  
1132 [Cattaneo, M., De Gori, P., Chiarabba, C., Monachesi, G., Lombardi, A., Valoroso, L.,](#)  
1133 [Latorre, D., & Marzorati, S. \(2017\). The 2016 Central Italy Seismic Sequence: A First](#)  
1134 [Look at the Mainshocks, Aftershocks, and Source Models. \*Seismological Research\*](#)  
1135 [Letters, 88\(3\), 757–771. <https://doi.org/10.1785/0220160221>](#)
- 1136 [Chiaraluca, L., Ellsworth, W. L., Chiarabba, C., & Cocco, M. \(2003\). Imaging the](#)  
1137 [complexity of an active normal fault system: The 1997 Colfiorito \(central Italy\) case](#)  
1138 [study. \*Journal of Geophysical Research: Solid Earth\*, 108\(B6\).](#)  
1139 <https://doi.org/10.1029/2002JB002166>
- 1140 Clavell, E., & Berastegui, X. (1991). Petroleum geology of the Gulf of Valencia. *Generation,*  
1141 *Accumulation, and Production of Europe's Hydrocarbons*, , 355–368.  
1142 [https://www.scopus.com/inward/record.uri?eid=2-s2.0-](https://www.scopus.com/inward/record.uri?eid=2-s2.0-0026310072&partnerID=40&md5=8f34c3d495738519a9101eb775a91bd4)  
1143 [0026310072&partnerID=40&md5=8f34c3d495738519a9101eb775a91bd4](https://www.scopus.com/inward/record.uri?eid=2-s2.0-0026310072&partnerID=40&md5=8f34c3d495738519a9101eb775a91bd4)
- 1144 De Ruig, & M.J. (1992). *Tectono-sedimentary evolution of the Prebetic fold belt of Alicante*
- 1145 Del Rio, V. D., Rey, J., & Vegas, R. (1986). The Gulf of Valencia continental shelf:  
1146 Extensional tectonics in Neogene and Quaternary sediments. *Marine Geology*, 73(1),  
1147 169–179. 10.1016/0025-3227(86)90117-9
- 1148 DeMets, C., Gordon, R. G., Argus, D. F., & Stein, S. (1994). Effect of recent revisions to the  
1149 geomagnetic reversal time scale on estimates of current plate motions. *Geophysical*  
1150 *Research Letters*, 21(20), 2191–2194. 10.1029/94GL02118
- 1151 Duffy, O. B., Gawthorpe, R. L., & Docherty, M. (2023). Tectono-stratigraphic evolution of  
1152 salt-influenced normal fault systems: an example from the Coffee-Soil Fault, Danish  
1153 North Sea. *Journal of the Geological Society*, 180(6), 1. 10.1144/jgs2023-016

Código de campo cambiado

- 1154 Etheve, N., Frizon de Lamotte, D., Mohn, G., Martos, R., Roca, E., & Blanpied, C. (2016).  
1155        Extensional vs contractional Cenozoic deformation in Ibiza (Balearic Promontory,  
1156        Spain): Integration in the West Mediterranean back-arc setting. *Tectonophysics*, 682,  
1157        35–55. 10.1016/j.tecto.2016.05.037
- 1158 Faccenna, C., Piromallo, C., Crespo-Blanc, A., Jolivet, L., & Rossetti, F. (2004a). Lateral  
1159        slab deformation and the origin of the western Mediterranean arcs. *Tectonics*  
1160        (*Washington, D.C.*), 23(1), np–n/a. 10.1029/2002TC001488
- 1161 Faccenna, C., Piromallo, C., Crespo-Blanc, A., Jolivet, L., & Rossetti, F. (2004b). Lateral  
1162        slab deformation and the origin of the western Mediterranean arcs. *Tectonics*  
1163        (*Washington, D.C.*), 23(1), np–n/a. 10.1029/2002TC001488
- 1164 Fang, P., Tugend, J., Mohn, G., Kusznir, N., & Ding, W. (2021a). Evidence for rapid large-  
1165        amplitude vertical motions in the Valencia Trough (Western Mediterranean)  
1166        generated by 3D subduction slab roll-back. *Earth and Planetary Science Letters*, 575,  
1167        117179. 10.1016/j.epsl.2021.117179
- 1168 Fang, P., Tugend, J., Mohn, G., Kusznir, N., & Ding, W. (2021b). Evidence for rapid large-  
1169        amplitude vertical motions in the Valencia Trough (Western Mediterranean)  
1170        generated by 3D subduction slab roll-back. *Earth and Planetary Science Letters*, 575,  
1171        117179. 10.1016/j.epsl.2021.117179
- 1172 Ford, M., Le Carlier de Veslud, C., & Bourgeois, O. (2007). Kinematic and geometric  
1173        analysis of fault-related folds in a rift setting: The Dannemarie basin, Upper Rhine  
1174        Graben, France. *Journal of Structural Geology*, 29(11), 1811–1830.  
1175        10.1016/j.jsg.2007.08.001

- 1176 García-Mayordomo, J., Insua-Arévalo, J. M., Martínez-Díaz, J. J., Jiménez-Díaz, A., Martín-  
1177 Banda, R., Martín-Alfageme, S., Álvarez-Gómez, J. A., Rodríguez-Peces, M., Pérez-  
1178 López, R., Rodríguez-Pascua, M. A., Masana, E., Perea, H., Martín-González, F.,  
1179 Giner-Robles, J., Nemser, E. S., & Cabral, J. (2012). The Quaternary active faults  
1180 database of Iberia (QAFI v. 2.0). *Journal of Iberian Geology*,  
1181 38(1)10.5209/rev\_JIGE.2012.v38.n1.39219
- 1182 Gaspar-Escribano, J. M., Garcia-Castellanos, D., Roca, E., & Cloetingh, S. (2004).  
1183 Cenozoic vertical motions of the Catalan Coastal Ranges (NE Spain): The role of  
1184 tectonics, isostasy, and surface transport. *Tectonics (Washington, D. C.)*, 23(1), np-  
1185 n/a. 10.1029/2003TC001511
- 1186 Geel, T. (1995). Oligocene to early Miocene tectono-sedimentary history of the Alicante  
1187 region (SE Spain): implications for Western Mediterranean evolution. *Basin Research*,  
1188 7(4), 313–336. 10.1111/j.1365-2117.1995.tb00120.x
- 1189 Geller, R. J. (1976). Scaling relations for earthquake source parameters and magnitudes.  
1190 *Bulletin of the Seismological Society of America*, 66(5), 1501–1523.  
1191 <https://pubs.geoscienceworld.org/ssa/bssa/article/66/5/1501/117604>
- 1192 González, Á. (2017). The Spanish National Earthquake Catalogue: Evolution, precision and  
1193 completeness. *Journal of Seismology*, 21(3), 435–471. 10.1007/s10950-016-9610-8
- 1194 Guimera, J., & Alvaro, M. (1990). Structure et évolution de la compression alpine dans la  
1195 Chaîne ibérique et la Chaîne côtière catalane (Espagne). *Bulletin De La Société*  
1196 *Géologique De France*, 6(2), 339–348. 10.2113/gssgfbull.VI.2.339

Con formato: Inglés (Estados Unidos)

Código de campo cambiado

1197 Hongxing, G., & Anderson, J. K. (2007). Fault throw profile and kinematics of Normal fault:  
1198 conceptual models and geologic examples. *Geological Journal of China Universities*,  
1199 13(1), 75.

1200 Huang, J., Abrahamson, N. A., Sung, C., & Chao, S. (2024). New Empirical Source-Scaling  
1201 Laws for Crustal Earthquakes Incorporating Fault Dip and Seismogenic-Thickness  
1202 Effects. *Seismological Research Letters*, 95(4), 2352–2367. 10.1785/0220240034

1203 Hyndman, R. D., Yamano, M., & Oleskevich, D. A. (1997). The seismogenic zone of  
1204 subduction thrust faults. *Island Arc*, 6(3), 244–260. 10.1111/j.1440-  
1205 1738.1997.tb00175.x

Con formato: Italiano (Italia)

1206 [Improta, L., Latorre, D., Margheriti, L., Nardi, A., Marchetti, A., Lombardi, A. M., Castello,](#)  
1207 [B., Villani, F., Ciaccio, M. G., Mele, F. M., Moretti, M., Battelli, P., Berardi, M.,](#)  
1208 [Castellano, C., Melorio, C., Modica, G., Pirro, M., Rossi, A., Thermes, C., .... Di Maro,](#)  
1209 [R. \(2019\). Multi-segment rupture of the 2016 Amatrice-Visso-Norcia seismic](#)  
1210 [sequence \(central Italy\) constrained by the first high-quality catalog of Early](#)  
1211 [Aftershocks. Scientific Reports, 9\(1\), 6921. https://doi.org/10.1038/s41598-019-](#)  
1212 [43393-2](#)

Con formato: Inglés (Estados Unidos)

1213 IGN. (2025). *Instituto Geográfico Nacional (2025) Servicio de Información Sísmica*.

1214 Jackson, C. A. -, & Rotevatn, A. (2013). 3D seismic analysis of the structure and evolution  
1215 of a salt-influenced normal fault zone: A test of competing fault growth models.  
1216 *Journal of Structural Geology*, 54, 215–234. 10.1016/j.jsg.2013.06.012

1217 Jackson, M. P. A., & Hudec, M. R. (2005). Stratigraphic record of translation down ramps in  
1218 a passive-margin salt detachment. *Journal of Structural Geology*, 27(5), 889–911.  
1219 10.1016/j.jsg.2005.01.010

- 1220 Jolivet, L., & Faccenna, C. (2000). Mediterranean extension and the Africa-Eurasia  
1221 collision. *Tectonics*, 19(6), 1095–1106. 10.1029/2000TC900018
- 1222 Kanamori, H., & Anderson, D. L. (1975). Theoretical basis of some empirical relations in  
1223 seismology. *Bulletin of the Seismological Society of America*, 65(5), 1073–1095.  
1224 <https://pubs.geoscienceworld.org/ssa/bssa/article/65/5/1073/117458>
- 1225 Kane, K. E., Jackson, C. A. -, & Larsen, E. (2010). Normal fault growth and fault-related  
1226 folding in a salt-influenced rift basin: South Viking Graben, offshore Norway. *Journal*  
1227 *of Structural Geology*, 32(4), 490–506. 10.1016/j.jsg.2010.02.005
- 1228 Leonard, M. (2010). Earthquake fault scaling; self-consistent relating of rupture length,  
1229 width, average displacement, and moment release. *Bulletin of the Seismological*  
1230 *Society of America*, 100(5A), 1971–1988. 10.1785/0120090189
- 1231 Leonard, M. (2014). Self-consistent earthquake fault-scaling relations; update and  
1232 extension to stable continental strike-slip faults. *Bulletin of the Seismological Society*  
1233 *of America*, 104(6), 2953–2965. 10.1785/0120140087
- 1234 Lirer, F., Foresi, L. M., Iaccarino, S. M., Salvatorini, G., Turco, E., Cosentino, C., Sierro, F.  
1235 J., & Caruso, A. (2019). Mediterranean Neogene planktonic foraminifer biozonation  
1236 and biochronology. *Earth-Science Reviews*, 196, 102869.  
1237 10.1016/j.earscirev.2019.05.013
- 1238 Lofi, J. (2011). *Seismic atlas of the "Messinian salinity crisis" markers in the Mediterranean*  
1239 *and Black Seas*. Commission for the Geological Map of the World.

Código de campo cambiado

- 1240 Maillard, A., Mauffret, A., Watts, A. B., Torné, M., Pascal, G., Buhl, P., & Pinet, B. (1992).  
1241 Tertiary sedimentary history and structure of the Valencia trough (western  
1242 Mediterranean). *Tectonophysics*, 203(1), 57–75. 10.1016/0040-1951(92)90215-R
- 1243 Maillard, A., & Mauffret, A. (2013). Structure and present-day compression in the offshore  
1244 area between Alicante and Ibiza Island (Eastern Iberian Margin). *Tectonophysics*,  
1245 591, 116–130. 10.1016/j.tecto.2011.07.007
- 1246 Mansfield, C. S., & Cartwright, J. A. (1996). High resolution fault displacement mapping  
1247 from three-dimensional seismic data: evidence for dip linkage during fault growth.  
1248 *Journal of Structural Geology*, 18(2), 249–263. 10.1016/S0191-8141(96)80048-4
- 1249 Marsh, N., Imber, J., Holdsworth, R. E., Brockbank, P., & Ringrose, P. (2010). The structural  
1250 evolution of the Halten Terrace, offshore Mid-Norway: extensional fault growth and  
1251 strain localisation in a multi-layer brittle-ductile system. *Basin Research*, 22(2), 195–  
1252 214. 10.1111/j.1365-2117.2009.00404.x
- 1253 Martí, J., Mitjavila, J., Roca, E., & Aparicio, A. (1992). Cenozoic magmatism of the valencia  
1254 trough (western mediterranean): Relationship between structural evolution and  
1255 volcanism. *Tectonophysics*, 203(1), 145–165. 10.1016/0040-1951(92)90221-Q
- 1256 Martínez-Solares, J. M., & Mezcua, J. (2002). *Catálogo sísmico de la Península Ibérica*.  
1257 Madrid (Spain): Instituto Geográfico Nacional.
- 1258 [Martinis, B., & Pieri, M. \(1969\). Alcune informazioni sulla formazione evaporitica del](#)  
1259 [Triassico superiore nell'Italia centrale meridionale. Memorie Della Società Geologica](#)  
1260 [Italiana, 4, 649–678.](#)

Con formato: Italiano (Italia)

- 1261 Maurin, J., & Niviere, B. (1999). Extensional forced folding and décollement of the pre-rift  
1262 series along the Rhine graben and their influence on the geometry of the syn-rift  
1263 sequences. *Forced Folds and Fractures* (pp. 73–86). The Geological Society of  
1264 London. 10.1144/GSL.SP.2000.169.01.06
- 1265 McClusky, S., Reilinger, R., Mahmoud, S., Ben Sari, D., & Tealeb, A. (2003). GPS  
1266 constraints on Africa (Nubia) and Arabia plate motions. *Geophysical Journal  
1267 International*, 155(1), 126–138. 10.1046/j.1365-246X.2003.02023.x
- 1268 [Michele, M., Chiaraluca, L., Di Stefano, R., & Waldhauser, F. \(2020\). Fine-Scale Structure  
1269 of the 2016–2017 Central Italy Seismic Sequence From Data Recorded at the Italian  
1270 National Network. \*Journal of Geophysical Research: Solid Earth\*, 125\(4\).  
1271 <https://doi.org/10.1029/2019JB018440>](#)
- 1272 Molinaro, M., Leturmy, P., Guezou, J. -, Frizon de Lamotte, D., & Eshraghi, S. A. (2005).  
1273 The structure and kinematics of the southeastern Zagros fold-thrust belt, Iran: From  
1274 thin-skinned to thick-skinned tectonics. *Tectonics*, 24(3), np–n/a.  
1275 10.1029/2004TC001633
- 1276 Morley, C. K., Back, S., Van Rensbergen, P., Crevello, P., & Lambiase, J. J. (2003).  
1277 Characteristics of repeated, detached, Miocene–Pliocene tectonic inversion events,  
1278 in a large delta province on an active margin, Brunei Darussalam, Borneo. *Journal of  
1279 Structural Geology*, 25(7), 1147–1169. 10.1016/S0191-8141(02)00130-X
- 1280 NEBOT, M., & GUIMERÀ, J. (2018). Kinematic evolution of a fold-and-thrust belt developed  
1281 during basin inversion: the Mesozoic Maestrat basin, E Iberian Chain. *Geological  
1282 Magazine*, 155(3), 630–640. 10.1017/S001675681600090X

- 1283 Nicol, A., Watterson, J., Walsh, J. J., & Childs, C. (1996). The shapes, major axis  
1284 orientations and displacement patterns of fault surfaces. *Journal of Structural*  
1285 *Geology*, 18(2), 235–248. 10.1016/S0191-8141(96)80047-2
- 1286 Nissen, E., Ghorashi, M., Jackson, J., Parsons, B., & Talebian, M. (2007). The 2005 Qeshm  
1287 Island earthquake (Iran)—a link between buried reverse faulting and surface folding  
1288 in the Zagros Simply Folded Belt? *Geophysical Journal International*, 171(1), 326–338.  
1289 10.1111/j.1365-246X.2007.03514.x
- 1290 Nissen, E., Tatar, M., Jackson, J. A., & Allen, M. B. (2011). New views on earthquake  
1291 faulting in the Zagros fold-and-thrust belt of Iran. *Geophysical Journal International*,  
1292 186(3), 928–944. 10.1111/j.1365-246X.2011.05119.x
- 1293 Nocquet, J. -, & Calais, E. (2003). Crustal velocity field of western Europe from permanent  
1294 GPS array solutions, 1996–2001. *Geophysical Journal International*, 154(1), 72–88.  
1295 10.1046/j.1365-246X.2003.01935.x
- 1296 Nocquet, J. (2012). Present-day kinematics of the Mediterranean: A comprehensive  
1297 overview of GPS results. *Tectonophysics*, 579, 220–242. 10.1016/j.tecto.2012.03.037
- 1298 Palano, M., González, P. J., & Fernández, J. (2015). The Diffuse Plate boundary of Nubia  
1299 and Iberia in the Western Mediterranean: Crustal deformation evidence for viscous  
1300 coupling and fragmented lithosphere. *Earth and Planetary Science Letters*, 430, 439–  
1301 447. 10.1016/j.epsl.2015.08.040
- 1302 Pascal, G., Torné, M., Buhl, P., Watts, A. B., & Mauffret, A. (1992). Crustal and velocity  
1303 structure of the Valencia trough (western Mediterranean), Part II. Detailed  
1304 interpretation of five Expanded Spread Profiles. *Tectonophysics*, 203(1), 21–35.  
1305 10.1016/0040-1951(92)90213-P

- 1306 Pascoe, R., Hooper, R., Storhaug, K., & Harper, H. (Jan 1, 1999). Evolution of extensional  
1307 styles at the southern termination of the Nordland Ridge, Mid-Norway: a response to  
1308 variations in coupling above Triassic salt. Paper presented at the , 5(1) 83–90.  
1309 10.1144/0050083 <https://www.lyellcollection.org/doi/10.1144/0050083>
- 1310 Perea, H. (2006). *Falles actives i perillositat sísmica al marge nord-occidental del solc de*  
1311 *València*
- 1312 Pérez-Peña, A., Martín-Davila, J., Gárate, J., Berrocoso, M., & Buforn, E. (2010). Velocity  
1313 field and tectonic strain in Southern Spain and surrounding areas derived from GPS  
1314 episodic measurements. *Journal of Geodynamics*, 49(3), 232–240.  
1315 10.1016/j.jog.2010.01.015
- 1316 Ramos, A., Lopez-Mir, B., Wilson, E. P., Granado, P., & Muñoz, J. A. (2020). 3D  
1317 reconstruction of syn-tectonic strata in a salt-related orogen: learnings from the Lleret  
1318 syncline (South-central Pyrenees). *Acta Geologica Hispanica*, 18(1), 1–19.  
1319 10.1344/GeologicaActa2020.18.20
- 1320 Ramos, A., de Ruig, M. J., Pedrera, A., Alfaro, P., & Martin-Rojas, I. (2025). Salt expulsion  
1321 triggered by prograding clinoforms in the SW Valencia Trough (SE Spain). *Marine and*  
1322 *Petroleum Geology*, 173, 107268. 10.1016/j.marpetgeo.2024.107268
- 1323 Ramos, A., Pedrera, A., García-Senz, J., López-Mir, B., & Salas, R. (2023). Seismic  
1324 evidence for ductile necking of the mid-lower crust beneath the Columbrets Basin  
1325 (Western Mediterranean). *Terra Nova (Oxford, England)*, 35(5), 404–412.  
1326 10.1111/ter.12664
- 1327 Rehault, J., Boillot, G., & Mauffret, A. (1984). The Western Mediterranean Basin geological  
1328 evolution. *Marine Geology*, 55(3), 447–477. 10.1016/0025-3227(84)90081-1

Código de campo cambiado

- 1329 Ribó, M., Puig, P., Muñoz, A., Lo Iacono, C., Masqué, P., Palanques, A., Acosta, J., Guillén,  
1330 J., & Gómez Ballesteros, M. (2016a). Morphobathymetric analysis of the large fine-  
1331 grained sediment waves over the Gulf of Valencia continental slope (NW  
1332 Mediterranean). *Geomorphology*, 253, 22–37. 10.1016/j.geomorph.2015.09.027
- 1333 Ribó, M., Puig, P., Urgeles, R., Van Rooij, D., & Muñoz, A. (2016b). Spatio-temporal  
1334 evolution of sediment waves developed on the Gulf of Valencia margin (NW  
1335 Mediterranean) during the Plio-Quaternary. *Marine Geology*, 378, 276–291.  
1336 10.1016/j.margeo.2015.11.011
- 1337 Richardson, N. J., Underhill, J. R., & Lewis, G. (2005). The role of evaporite mobility in  
1338 modifying subsidence patterns during normal fault growth and linkage, Halten  
1339 Terrace, Mid-Norway. *Basin Research*, 17(2), 203–223. 10.1111/j.1365-  
1340 2117.2005.00250.x
- 1341 Roca, E. (1994). La evolución geodinámica de la Cuenca Catalano-Balear y áreas  
1342 adyacentes desde el Mesozoico hasta la actualidad. *Acta Geologica Hispanica*,  
1343 29(1), 3–25. <https://raco.cat/index.php/ActaGeologica/article/view/75462>
- 1344 Roca, E. (2001). The Northwest Mediterranean Basin (Valencia Trough, Gulf of Lions and  
1345 Liguro-Provençal basins): structure and geodynamic evolution. *Mem. Mus. Natl. Hist.*  
1346 *Nat. (France)* (pp. 671–706)
- 1347 Roca, E., Frizon de Lamotte, D., Mauffret, A., Bracene, R., Verges, J., Benaouali, N.,  
1348 Fernandez, M., Muñoz, J. A., & Zeyen, H. (2004). TRANSMED-transect II (Aquitaine  
1349 basin, Pyrenees, Ebro basin, Catalan coastal ranges, Valencia trough, Balearic  
1350 promontory, Algerian basin, Tell, Sahara Atlas, Sahara platform). In : W. Cavazza, F.  
1351 Roure, W. Spakman, G.M. Stampfli and P.A. Ziegler (Eds). The TRANSMED Atlas - the

Código de campo cambiado

- 1352 Mediterranean region from Crust to Mantle. *Springer, Berlin* <https://hal.science/hal->  
1353 [00069583](https://hal.science/hal-00069583)
- 1354 Roca, E., & Desegaulx, P. (1992). Analysis of the geological evolution and vertical  
1355 movements in the València Trough area, western Mediterranean. *Marine and*  
1356 *Petroleum Geology*, 9(2), 167,IN1,177–176,IN8,185. 10.1016/0264-8172(92)90089-W
- 1357 Roca, E., & Guimerà, J. (1992). The Neogene structure of the eastern Iberian margin:  
1358 Structural constraints on the crustal evolution of the Valencia trough (western  
1359 Mediterranean). *Tectonophysics*, 203(1), 203–218. 10.1016/0040-1951(92)90224-T
- 1360 Roca, E., Sans, M., Cabrera, L., & Marzo, M. (1999). Oligocene to Middle Miocene  
1361 evolution of the central Catalan margin (northwestern Mediterranean).  
1362 *Tectonophysics*, 315(1), 209–229. 10.1016/S0040-1951(99)00289-9
- 1363 Rouby, D., Guillocheau, F., Robin, C., Bouroullec, R., Raillard, S., Castelltort, S., & Nalpas,  
1364 T. (2003). Rates of deformation of an extensional growth fault/raft system (offshore  
1365 Congo, West African margin) from combined accommodation measurements and 3-  
1366 D restoration. *Basin Research*, 15(2), 183–200. 10.1046/j.1365-2117.2003.00200.x
- 1367 Roustaei, M., Nissen, E., Abbassi, M., Gholamzadeh, A., Ghorashi, M., Tatar, M., Yamini-  
1368 Fard, F., Bergman, E., Jackson, J., & Parsons, B. (2010). The 2006 March 25 Fin  
1369 earthquakes (Iran)—insights into the vertical extents of faulting in the Zagros Simply  
1370 Folded Belt. *Geophysical Journal International*, 181(3), 1275–1291. 10.1111/j.1365-  
1371 246X.2010.04601.x
- 1372 [Rovida, A., Locati, M., Camassi, R., Lolli, B., & Gasperini, P. \(2020\). The Italian earthquake](#)  
1373 [catalogue CPTI15. \*Bulletin of Earthquake Engineering\*, 18\(7\), 2953–2984.](#)  
1374 <https://doi.org/10.1007/s10518-020-00818-y>

Código de campo cambiado

- 1375 Ruff, L., & Kanamori, H. (1983). Seismic coupling and uncoupling at subduction zones.  
1376 *Tectonophysics*, 99(2), 99–117. 10.1016/0040-1951(83)90097-5
- 1377 Ruig, M. J. d. (1996). Extensional diapirism in the eastern Prebetic foldbelt, southeastern  
1378 Spain. *AAPG Memoir*, (65) <https://www.osti.gov/biblio/585188>
- 1379 Sàbat, F., Gelabert, B., Rodríguez-Perea, A., & Giménez, J. (2011). Geological structure  
1380 and evolution of Majorca: Implications for the origin of the Western Mediterranean.  
1381 *Tectonophysics*, 510(1), 217–238. 10.1016/j.tecto.2011.07.005
- 1382 Salas, R., Guimera, J., Mas, R., Martin-Closas, C., Melendez, A., & Alonso, A. (2001a).  
1383 Evolution of the Mesozoic Central Iberian Rift System and its Cainozoic inversion  
1384 (Iberian chain). *Mémoires Du Muséum National D'histoire Naturelle (1993)*, 186, 145–  
1385 186.
- 1386 SaAlas, R., Guimera, J., Mas, R., Martin-Closas, C., Melendez, A., & Alonso, A. (2001b).  
1387 Evolution of the Mesozoic Central Iberian Rift System and its Cainozoic inversion  
1388 (Iberian chain). *Mémoires Du Muséum National D'histoire Naturelle (1993)*, 186, 145–  
1389 186.
- 1390 Seranne, M. (1999). The Gulf of Lion continental margin (NW Mediterranean) revisited by  
1391 IBS: an overview. *Geological Society special publication* (pp. 15–36). The Geological  
1392 Society of London. 10.1144/GSL.SP.1999.156.01.03
- 1393 Serpelloni, E., Vannucci, G., Pondrelli, S., Argnani, A., Casula, G., Anzidei, M., Baldi, P., &  
1394 Gasperini, P. (2007). Kinematics of the Western Africa-Eurasia plate boundary from  
1395 focal mechanisms and GPS data. *Geophysical Journal International*, 169(3), 1180–  
1396 1200. 10.1111/j.1365-246X.2007.03367.x

Con formato: Español (España)

- 1397 Sherkati, S., Molinaro, M., Frizon de Lamotte, D., & Letouzey, J. (2005). Detachment  
1398 folding in the Central and Eastern Zagros fold-belt (Iran): salt mobility, multiple  
1399 detachments and late basement control. *Journal of Structural Geology*, 27(9), 1680–  
1400 1696. 10.1016/j.jsg.2005.05.010
- 1401 Soler y José, R., Martínez del Olmo, W., Megías, A. G., & Abeger Monteagudo, J. A. (1983).  
1402 Rasgos básicos del neógeno del Mediterráneo español. *Mediterránea. Serie de*  
1403 *Estudios Geológicos*, 1, 71–82.
- 1404 Stampfli, G. M., & Hocker, C. F. W. (1989). Messinian palaeorelief from a 3-D seismic  
1405 survey in the Tarraco concession area (Spanish Mediterranean Sea). *Geologie En*  
1406 *Mijnbouw*, 68(2), 201–210.
- 1407 Stewart, S. A., Ruffell, A. H., & Harvey, M. J. (1997). Relationship between basement-linked  
1408 and gravity-driven fault systems in the UKCS salt basins. *Marine and Petroleum*  
1409 *Geology*, 14(5), 581–604. 10.1016/S0264-8172(97)00008-1
- 1410 Stich, D., Martín, R., & Morales, J. (2010). *Moment tensor inversion for Iberia-Maghreb*  
1411 *earthquakes 2005-2008*. Elsevier.
- 1412 Stich, D., Serpelloni, E., de Lis Mancilla, F., & Morales, J. (2006). Kinematics of the Iberia–  
1413 Maghreb plate contact from seismic moment tensors and GPS observations.  
1414 *Tectonophysics*, 426(3), 295–317. 10.1016/j.tecto.2006.08.004
- 1415 Stirling, M., Goded, T., Berryman, K., & Litchfield, N. (2013). Selection of earthquake  
1416 scaling relationships for seismic-hazard analysis. *Bulletin of the Seismological*  
1417 *Society of America*, 103(6), 2993–3011. 10.1785/0120130052

- 1418 Stirling, M., Rhoades, D., & Berryman, K. (2002). Comparison of earthquake scaling  
1419 relations derived from data of the instrumental and preinstrumental era. *Bulletin of*  
1420 *the Seismological Society of America*, 92(2), 812–830. 10.1785/0120000221
- 1421 Stock, C., & Smith, E. G. C. (2000). Evidence for different scaling of earthquake source  
1422 parameters for large earthquakes depending on faulting mechanism. *Geophysical*  
1423 *Journal International*, 143(1), 157–162. 10.1046/j.1365-246x.2000.00225.x
- 1424 Thorsen, C. E. (1963). Age of growth faulting in southeast Louisiana.
- 1425 Torné, M., Pascal, G., Buhl, P., Watts, A. B., & Mauffret, A. (1992). Crustal and velocity  
1426 structure of the Valencia trough (western Mediterranean), Part I. A combined  
1427 refraction/ wide-angle reflection and near-vertical reflection study. *Tectonophysics*,  
1428 203(1), 1–20. 10.1016/0040-1951(92)90212-O
- 1429 Tvedt, A. B. M., Rotevatn, A., Jackson, C. A. -, Fossen, H., & Gawthorpe, R. L. (2013).  
1430 Growth of normal faults in multilayer sequences: A 3D seismic case study from the  
1431 Egersund Basin, Norwegian North Sea. *Journal of Structural Geology*, 55, 1–20.  
1432 10.1016/j.jsg.2013.08.002
- 1433 [Valoroso, L., Chiaraluce, L., Piccinini, D., Di Stefano, R., Schaff, D., & Waldhauser, F.](#)  
1434 [\(2013\). Radiography of a normal fault system by 64,000 high-precision earthquake](#)  
1435 [locations: The 2009 L'Aquila \(central Italy\) case study. \*Journal of Geophysical\*](#)  
1436 [Research: Solid Earth](#), 118(3), 1156–1176. <https://doi.org/10.1002/jgrb.50130>
- 1437 van Hinsbergen, D. J. J., Torsvik, T. H., Schmid, S. M., Mañenco, L. C., Maffione, M.,  
1438 Vissers, R. L. M., Gürer, D., & Spakman, W. (2020). Orogenic architecture of the  
1439 Mediterranean region and kinematic reconstruction of its tectonic evolution since the  
1440 Triassic. *Gondwana Research*, 81, 79–229. 10.1016/j.gr.2019.07.009

- 1441 van Hinsbergen, D. J. J., Vissers, R. L. M., & Spakman, W. (2014). Origin and consequences  
1442 of western Mediterranean subduction, rollback, and slab segmentation. *Tectonics*  
1443 (*Washington, D.C.*), 33(4), 393–419. 10.1002/2013TC003349
- 1444 Vargas, H., Gaspar-Escribano, J. M., López-Gómez, J., Van Wees, J., Cloetingh, S., de La  
1445 Horra, R., & Arche, A. (2009). A comparison of the Iberian and Ebro Basins during the  
1446 Permian and Triassic, eastern Spain: A quantitative subsidence modelling approach.  
1447 *Tectonophysics*, 474(1), 160–183. 10.1016/j.tecto.2008.06.005
- 1448 Verges, J., & Sabat, F. (1999). Constraints on the Neogene Mediterranean kinematic  
1449 evolution along a 1000 km transect from Iberia to Africa. *Geological Society special*  
1450 *publication* (pp. 63–80). The Geological Society of London.  
1451 10.1144/GSL.SP.1999.156.01.05
- 1452 Verges, J., & Fernandez, M. (2012). Tethys–Atlantic interaction along the Iberia–Africa  
1453 plate boundary: The Betic–Rif orogenic system. *Tectonophysics*, 579, 144–172.  
1454 10.1016/j.tecto.2012.08.032
- 1455 Wells, D. L., & Coppersmith, K. J. (1994). New empirical relationships among magnitude,  
1456 rupture length, rupture width, rupture area, and surface displacement. *Bulletin of the*  
1457 *Seismological Society of America*, 84(4), 974–1002.  
1458 <https://pubs.geoscienceworld.org/ssa/bssa/article/84/4/974/119792>
- 1459 Weng, H., & Yang, H. (2017). Seismogenic width controls aspect ratios of earthquake  
1460 ruptures. *Geophysical Research Letters*, 44(6), 2725–2732. 10.1002/2016gl072168
- 1461 Withjack, M. O., & Callaway, S. (2000). Active normal faulting beneath a salt layer; an  
1462 experimental study of deformation patterns in the cover sequence. *AAPG Bulletin*,  
1463 84(5), 627–651. 10.1306/C9EBCE73-1735-11D7-8645000102C1865D

Código de campo cambiado

- 1464 Withjack, M. O., Olson, J., & Peterson, E. (1990). Experimental models of extensional  
1465 forced folds. *AAPG Bulletin*, 74(7), 1038–1054. 10.1306/OC9B23FD-1710-11D7-  
1466 8645000102C1865D
- 1467 Yen, Y., & Ma, K. (2011a). Source-scaling relationship for M 4.6-8.9 earthquakes,  
1468 specifically for earthquakes in the collision zone of Taiwan. *Bulletin of the*  
1469 *Seismological Society of America*, 101(2), 464–481. 10.1785/0120100046
- 1470 Yen, Y., & Ma, K. (2011b). Source-scaling relationship for M 4.6-8.9 earthquakes,  
1471 specifically for earthquakes in the collision zone of Taiwan. *Bulletin of the*  
1472 *Seismological Society of America*, 101(2), 464–481. 10.1785/0120100046
- 1473 Zazo, C. (1979). El problema del límite Plio-Pleistoceno en el litoral S y SE de España.  
1474 *Trabajos N/Q*, 9, 65–72.
- 1475
- 1476
- 1477